Institute for Nuclear Research
Russian Academy of Sciences
60th October Anniversary Prospect, 7A
Moscow, 117 312, Russia

Conceptual Design
of a Positron Injector
for the TESLA Linear Collider

Working group:

INR

V.V. Balandin, N.I. Golubeva, L.V. Kravchuk, V.A. Moiseev, V.N. Mikhailov,
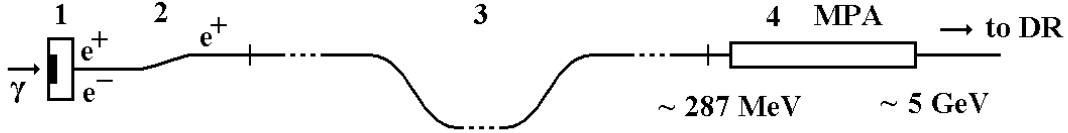V.V. Paramonov, P.I. Reinhardt-Nickoulin

DESY

K. Flöttmann

Edited by V.V. Paramonov, K. Flöttmann

Moscow-Hamburg, 2000

Contents

1. Conversion target + Adiabatic Matching Device

2. Positron Pre-Accelerator - PPA

3. Long Positron Transport Line - LPTL

4. Main Positron Accelerator

Figure 1.1: Schematic sketch of the Positron Injector

1   Introduction

The conceptual design of the TESLA 500 GeV electron-positron linear collider with integrated X-ray laser facility is presented in [1]. The collider will use the 250GeV electron beam before the Interaction Point (IP) to produce a positron beam, by passing the electron beam through a wiggler to produce photons, which will hit a thin target to yield the positrons.

Since the positrons have a broad distribution of transverse and longitudinal momenta they have to be accelerated in an acceleration section embedded in a solenoid field. The acceptance of a solenoid channel is characterized by a large spot size and small angles while the positrons emerging from the target have a small spot size and large angles. To match the positrons to the acceptance of the solenoid, an Adiabatic Matching Device (AMD) is used. It consists of a tapered solenoid field which starts with a higher initial field and tapers down adiabatically to the constant end field [1].

After the AMD the positron beam should be captured, pre-accelerated up to $\approx 250\,\mathrm{MeV}$ in the normal conducting Positron Pre-Accelerator (PPA) linac, transported with the Long Positron Transport Line (LPTL) to the superconducting Main Positron Accelerator linac (MPA), accelerated to $\approx 5\,\mathrm{GeV}$ and injected into the Damping Ring (DR).

The proposal of the PPA scheme is presented in [2] and in the present consideration we strongly refer to this work.

In this report we consider the parameters of the total positron injector channel (Fig. 1.1). Parameters of the PPA are revised taking into account both the results of coupled optimization PPA - AMD and the reasonable solution for the LPTL. The MPA scheme is proposed taking into account the enlarged positron beam emittance.

  The Chapters $2 \div 6$ describe mainly the way of investigations and scientific results, the Chapter 7 represent resulting proposals for all parts of a TESLA positron injector.

2   The coupled optimization of AMD and PPA

The general concept of the PPA was presented ealier in [2]. At the beginning of the PPA there is the AMD followed by the linear accelerator embedded in a solenoid field. The AMD is a special solenoid with combined pulsed and time constant magnetic fields [3]. Its on axis magnetic field is tapered by the law

$$B(s) = \frac{B_0}{1 + gs} \tag{1}$$

whith s - the longitudinal coordinate, B_0 - the maximum magnetic field, g - the taper coefficient.

We suppose that the final AMD field is equal to the constant magnetic field of the solenoid placed just behind the AMD. Depending on initial positron distribution, AMD parameters (B_0 and g), solenoid magnetic field B_{sol} and technical reasons there is an optimum of the capture efficiency for the useful part of the totally acceptable e^+ beam. In our case the reasonable value for B_0 is determined as 6 T [3]. And further we also suppose that the phase space distributions of the positrons and electrons emmited from the target have been preliminary defined [3] and the useful part of the positrons has

- an energy spread of $\pm 6\,\%$ for the PPA output energy $(250 \div 300)\,\mathrm{MeV}$;
- an rf-phase spread of $\pm 7.5^o$ for the PPA rf-frequency 1.3 GHz.

The capture efficiency is calculated as the ratio of the number of positrons in the useful part with required limitations in the transverse phase space to the total number of positrons escaped from the target. According to the previous studies [1], the total normalized transverse positron beam emittance should satisfy the condition $\varepsilon_x + \varepsilon_y \leq 0.048\,\mathrm{m}$. For further analysis the following requirements to the particle transverse phase space were introduced:

$$\text{Req.1} \qquad\qquad \varepsilon_x + \varepsilon_y \;\leq 0.048\,\mathrm{m} \tag{2}$$

$$\text{Req.2} \qquad\qquad
\begin{aligned}
\varepsilon_x &\leq 0.036\,\mathrm{m} \\
\varepsilon_y &\leq 0.036\,\mathrm{m} \\
\varepsilon_x + \varepsilon_y &\leq 0.048\,\mathrm{m}
\end{aligned} \tag{3}$$

$$\text{Req.3} \qquad\qquad
\begin{aligned}
\varepsilon_x &\leq 0.024\,\mathrm{m} \\
\varepsilon_y &\leq 0.024\,\mathrm{m}
\end{aligned} \tag{4}$$

It should be noted here, the higher the number the stronger the requirement is. It means that Req.1 contains both Req.2 and Req.3. Whereas Req.2 only includes Req.3.

In this paragraph the results of simulations are presented for a special PPA option, designed only with solenoid focusing [2], i.e. in this case the PPA accelerating sructure is fully embedded in a straight focusing solenoid. From our previous PPA studies [2] it can be concluded that both longitudinal and transverse structures of the positron beam mainly form up to $\sim 100\,\mathrm{MeV}$ energy. It means that the results of the coupled optimization of AMD and PPA with solenoid focusing are valid for the PPA with any transverse focusing schemes (FODO, doublets, triplets and so on) beyond the beam energy of 100 MeV.

The goal of the investigation is to estimate the influence of the free AMD parameters on

the PPA capture efficiency. The subjects of the optimization are:
- the AMD field taper coefficient g;
- the final AMD field B_{sol}, which is equal to the magnetic field in the PPA focusing solenoid;
- the entering length L_{ins} of the first rf-section into the AMD.

The last parameter must be specially commented. The pulsed part of the AMD with a strong magnetic field has a short length ($\sim (20 \div 30)$ cm)[3]. Whereas the time constant AMD part with a weak magnetic field has a length more than ~ 40 cm, depending on the parameter g. Putting the first rf-section into the AMD, the bunch lengthening due to a wide particle momentum spread in the AMD will be reduced. However, the AMD adiabaticity may be lost, which can lead to the positron losses in the focusing solenoid and, as a result, to a drop of the PPA positron capture efficiency.

At first the previous PPA design described in [2] has been studied. Some characteristic parameters were:
- the aperture diameter of the accelerating structure is 52 mm;
- the field strength of the focusing solenoid is 0.24 T;
- the AMD length is 0.8 m.

It should be noted here that the total normalized transverse emittance for the output positron beam was equal to ~ 0.05 m in both transverse planes. Therefore Reqs.(2) $\div$ (4) are valid for increasing parts of the positron beam.

The results of simulations are presented as contour levels for the AMD free parameters variations and rf-scanning in (Figs.2.1 $\div$ 2.3). The letter one was carried out with respect to a test particle emitted from the target with a kinetic energy of 7 MeV without a transverse moment and traversing the first gap centre of the first rf-section with the rf-phase plotted on these figures.

The results of the simulations can be formulated as follows:
- there is an optimum for the AMD tapered parameter g. For the optimum g-value the capture efficiencies are slightly different for Req.1 (2) and Req.2 (3), whereas there is no essential difference for Req.3 (4);
- the higher final AMD magnetic field B_{sol} is better. But, with increasing field the growth rate for the capture efficiency slows down essentially;
- for the total range of the AMD entering parameter L_{ins} the evident optimum (maximum) wasn't reached for the capture efficiency which has a higher growth rate with L_{ins} increasing.

Summarizing the above conclusions the following AMD and PPA parameters can be confirmed for the previous PPA design [2]:
- AMD tapeted parameter $g = 30$ m^{-1};
- AMD final magnetic field $B_{sol} = 0.24$ T. This choice was made for technical reasons for the PPA focusing solenoid;
- according to dependence (1), the AMD length is 0.8 m;
- the AMD entering parameter is $L_{ins} = 0.6$ m, the value being approximate. Apparently, for the real construction, it may be recommended to put the first rf-section into the AMD as far as possible depending on the technical reasons.

For chosen AMD parameters and rf-phase $\sim (-22^o)$ we may expect the following estimations for the output positron beam:
- the capture efficiencies are $27.6\%, 26.5\%, 22.4\%$ for Req.1, Req.2 and Req.3, respectively;
- the average kinetic energy is ~ 247 MeV.
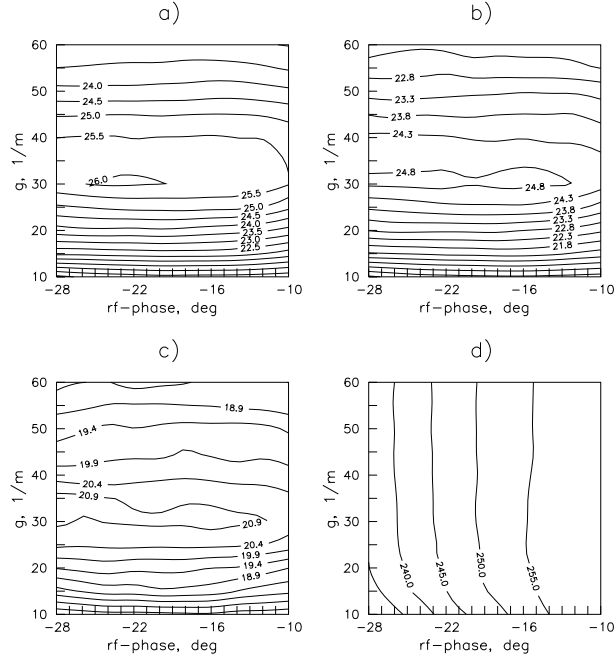
Figure 2.1: Capture efficiency (a, b, c) in % and output energy (d) in MeV levels for $B_{sol} = 0.24\,\mathrm{T}$ and $L_{ins} = 0\,\mathrm{m}$ in dependence from the AMD taper parameter g and rf-phase scanning. a) - for Req.1; b) - for Req.2; c) - for Req.3.

Figure 2.2: Capture efficiency (a, b, c) in % and output energy (d) in MeV levels for $g = 30\,\mathrm{m}^{-1}$ and $L_{ins} = 0\,\mathrm{m}$ in dependence from the AMD final magnetic field B_{sol} and rf-phase scanning. a) - for Req.1; b) - for Req.2; c) - for Req.3.

Figure 2.3: Capture efficiency (a, b, c) in % and output energy (d) in MeV levels for $g = 30\,\text{m}^{-1}$ and $B_{sol} = 0.24\,\text{T}$ in dependence from the entering length L_{ins} of the first rf-section into the AMD and rf-phase scanning. a) - for Req.1; b) - for Req.2; c) - for Req.3.

Following the above recommendations and results some simulations were carried out to improve the PPA operating parameters. It is evident that due to the small difference for the capture efficiencies for Req.1 and Req.2 it is not necessary to use a large rf-section iris diameter. Its reduction will diminish particle losses and beam power loading at the PPA beginning thus improving the PPA operation. Results of capture efficiency for different magnetic fields of the PPA focusing solenoid and inner aperture radius of the rf-sections are presented in (Fig2.4). For $B_{sol} = 0.24\,\text{T}$ it is obvious that without essential losses of the capture efficiency the iris radius of the rf-sections can be reduced up to $\sim 23\,\text{mm}$. Also, taking into account the weak dependence of the capture efficiency on the focusing magnetic field B_{sol} in the range more then $0.2\,\text{T}$ (Fig.2.2 and Fig.2.4 for $B_{sol} = 0.2\,\text{T}$), it can be recommended to use B_{sol} lower than $0.24\,\text{T}$, thus improving the solenoid DC power consumptions. For further study $B_{sol} = 0.22\,\text{T}$ and iris diameters of $47\,\text{mm}$ for the two first rf-sections and $46\,\text{mm}$ for the others were chosen. Moreover a new rf-section design and rf-feeding concept (see Chapter.3) have been used. The results of simulations are presented in Fig.2.5÷Fig.2.7.

Analizing these results, the results of the previous optimization and the above assumptions the final recommendations for the AMD and PPA design parameters are:
- the aperture diameters are $47\,\text{mm}$ for two first rf-sections and $46\,\text{mm}$ for the others;
- AMD taper parameter is $g = 29.5\,\text{m}^{-1}$;
- AMD final magnetic field is $B_{sol} = 0.22\,\text{T}$;
- according to dependence (1) the AMD length is $\sim 0.89\,\text{m}$;
- AMD entering parameter is $L_{ins} \sim 0.6\,\text{m}$.
For the chosen AMD parameters and rf-phase $\sim (-20^{\circ})$ we may expect the following
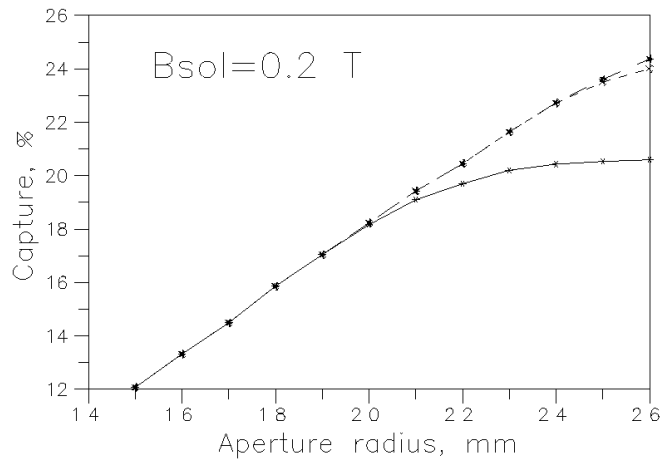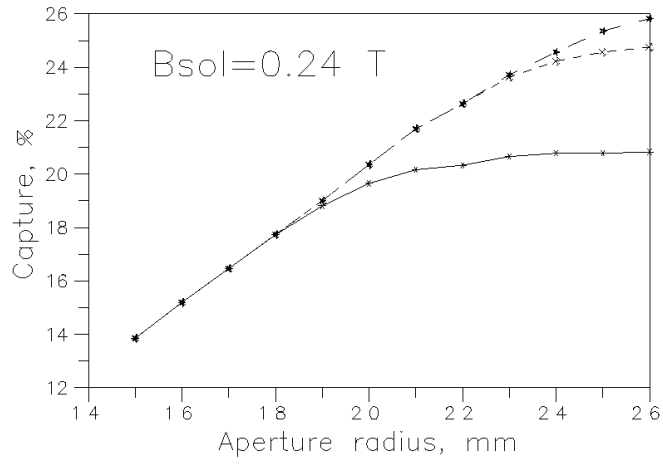
Figure 2.4: Capture efficiency for $g = 30\,\mathrm{m}^{-1}$ and $L_{ins} = 0\,\mathrm{m}$ in dependence of the rf-section iris for fixed rf-phase (-18°) - upper curve for Req.1; - middle curve for Req.2; - lower curve for Req.3.

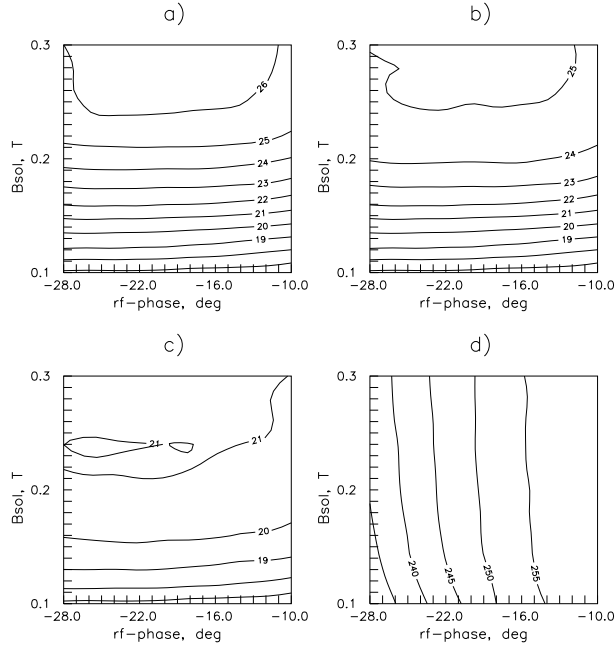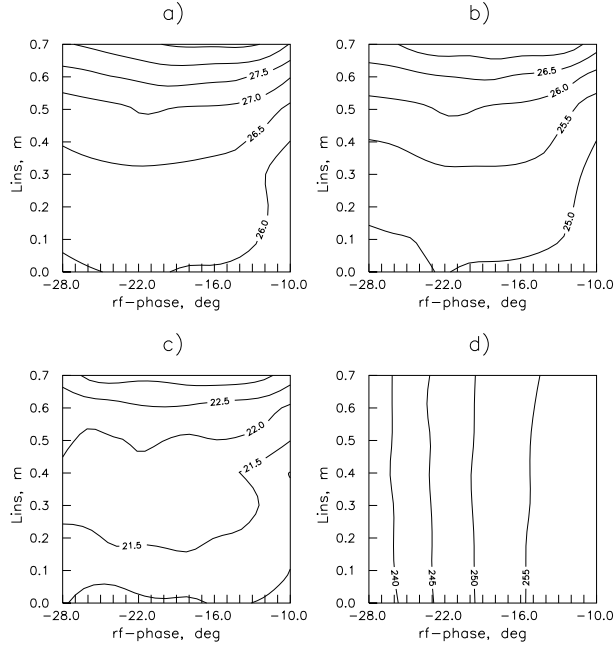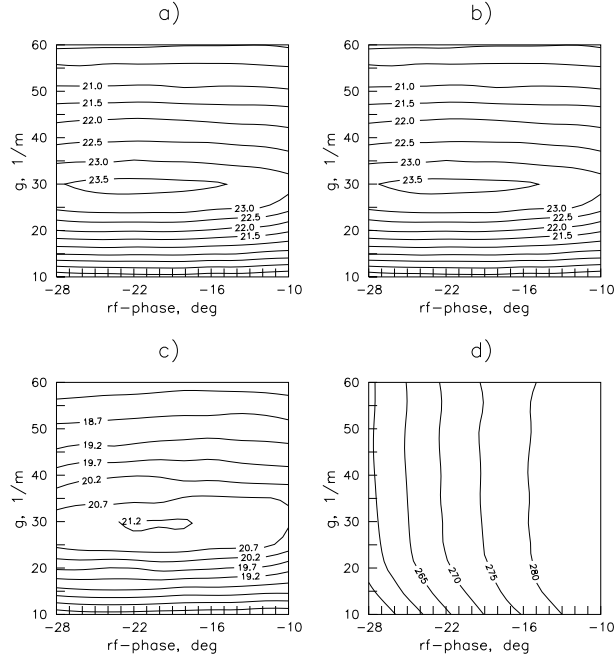Figure 2.5: Capture efficiency (a, b, c) in % and output energy (d) in MeV levels for $B_{sol} = 0.22\,\mathrm{T}$ and $L_{ins} = 0\,\mathrm{m}$ in dependence from the AMD taper parameter g and rf-phase scanning. a) - for Req.1; b) - for Req.2; c) - for Req.3.
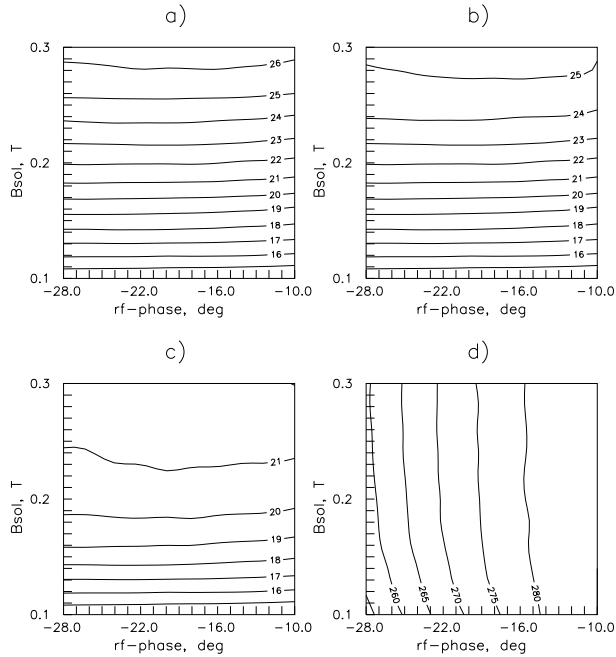
Figure 2.6: Capture efficiency (a, b, c) in % and output energy (d) in MeV levels for $g = 33\,\mathrm{m}^{-1}$ and $L_{ins} = 0\,\mathrm{m}$ in dependence from the AMD final magnetic field B_{sol} and rf-phase scanning. a) - for Req.1; b) - for Req.2; c) - for Req.3.

Figure 2.7: Capture efficiency (a, b, c) in % and output energy (d) in MeV levels for $g = 33\,\mathrm{m}^{-1}$ and $B_{sol} = 0.22\,\mathrm{T}$ in dependence from the entering length L_{ins} of the first rf-section into the AMD and rf-phase scanning. a) - for Req.1; b) - for Req.2; c) - for Req.3.

estimations for the output positron beam:
- the capture efficiencies are $24.8\%, 24.8\%, 22.5\%$ for Req.1, Req.2 and Req.3, respectively;
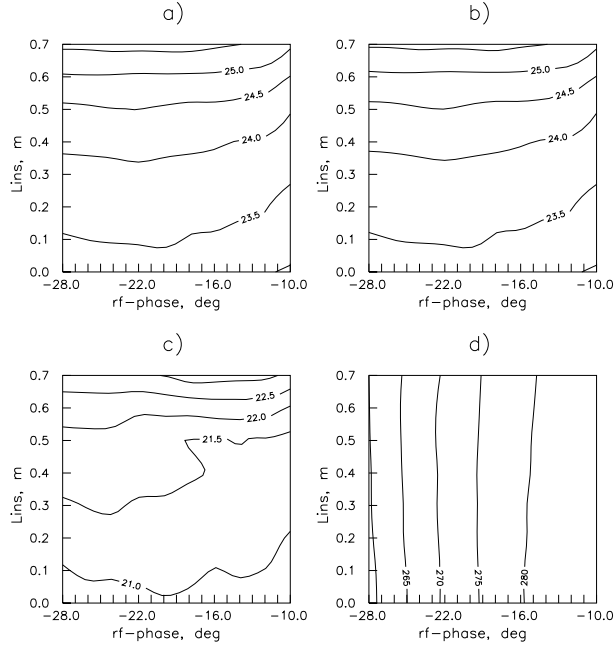- the average kinetic energy is $\sim 274\,\mathrm{MeV}$.

2.1 Summary

A coupled optimization of the parameters of the AMD and the PPA beginning has been performed. The results of this optimization a show small improvement in the capture efficiency. It confirms that the parameters of the PPA beginning were chosen reasonably in the previous design. The detailed study shows the possibility to restrict the PPA acceptance. The outer triangle parts of the transverse phase space with $\varepsilon_x + \varepsilon_y \leq 0.048\,\mathrm{m}, \varepsilon_x \geq 0.036\,\mathrm{m}, \varepsilon_y \geq 0.036\,\mathrm{m}$ are low populated with positrons. Without significant decreasing in the capture efficiency the Req. 2 for the positron beam emittance has been accepted for further consideration. Taking into account the long-distance beam transport between the PPA and the MPA and further acceleration in the superconducting Main Positron Accelerator, it is reasonable to restrict the beam emittance at the beginning of the positron injector. It releases the requirements to the hardware parameters for all parts of the injector and leads to a costs reduction practically without reduction in the total number of the accelerated positrons.
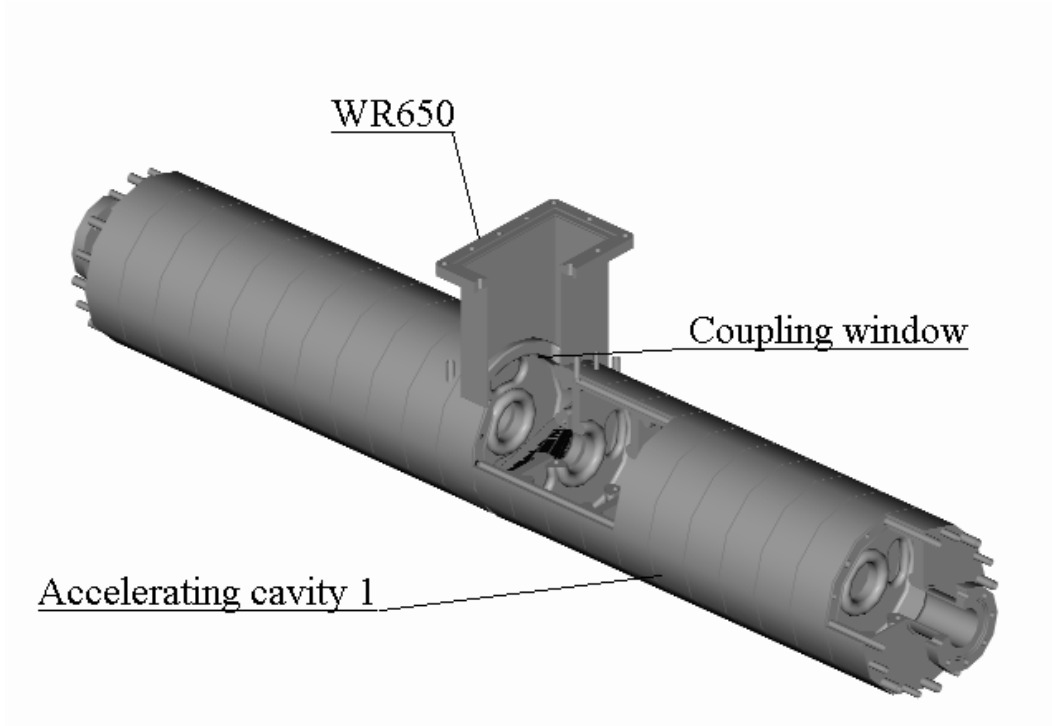
Figure 3.1.1: Short accelerating cavity in the first PPA part.

3   The PPA accelerating and RF system

The beam dynamic study for a total channel for positron acceleration, from the target to the damping ring results in the conclusion, that the PPA acceptance [2] has a reserve. Without significant reduction in the capture efficiency, this reserve may be reduced, leading to more comfortable conditions for technical systems operation.

Moreover, we consider a single drive option for the accelerating cavities, assuming the rf power from the two standard TESLA $10MW$ klystron outputs to be combined.

3.1   Updating PPA accelerating structure parameters

After a more detailed beam dynamics study (see Chapter 2) the aperture diameter for the PPA accelerating structure was reduced from $52mm$ [2] to $\approx 46mm$.

General features of the PPA accelerating structure are the same as described before [2]. The single drive option leads to another structure segmentation. The first part of the PPA has 4 Accelerating Cavities (AC) and, respectively, 4 rf channels. In the PPA beginning two short ACs (11 accelerating cells, Fig. 3.1.1) are designed for a high accelerating gradient $E_1T \approx 14.5MV/m$. The other two long ACs (37 accelerating cells) in the PPA first part and all the ACs in the PPA second part have $E_1T \approx 8.5MV/m$. (For E_1T definition see [2], Chapter 4.4.) The structure segmentation for the PPA second part is described in Chapter 3.3. The revised parameters (due to the aperture decreasing) for the Cut Disk Structure [4] cells are listed in Table 3.1.1. The values for the effective shunt
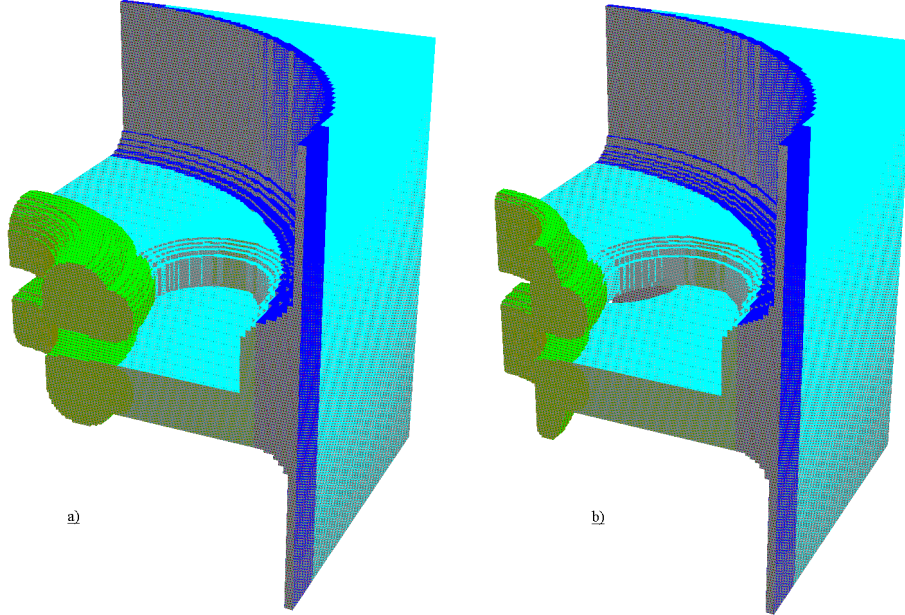
Figure 3.1.2: CDS accelerating cells for high (a) and moderate (b) gradient.

impedance Z_e and quality factor Q are reduced by 5% in comparison with 3D MAFIA results taking into account the usual difference in these parameters for cavities brazed with silver alloy.

A general view of the CDS cells is shown in Fig. 3.1.2 for the options with a high accelerating gradient $E_1T = 14.5MV/m$ (Fig. 3.1.2a) and for $E_1T = 8.5MV/m$ (Fig. 3.1.2b).

3.2 Bridge coupling cavities.

Due to the triplet focusing scheme, we cannot use long ACs in the PPA second part. The accelerating cavity should be broken in two accelerating sections and a triplet should be placed between sections. To combine sections into a joint resonant system and drive them from a single rf source, a coupling bridge cavity may be used.

Attractive features of the bridge coupled system are well known and have been proved experimentally for Coupled Cells accelerating Structures (CCS) at high frequencies ≈ 1000 MHz in several laboratories. With bridge couplers application the field distribution, in both amplitude and phase, is automatically stabilized among connected sections in the lowest order. Additional rf power dissipation of the order of several percent is inevitable in the bridge coupler because of its standing-wave operation.

Coupling with intermediate coupling cell. The TM_{010} mode post stabilized Cylindrical Bridge Cavities (CBC) were proposed in [5] and realized in the accelerating system of the LANL $800MeV$ proton linac together with the Side Coupled accelerating structure.

13

Table 3.1.1: CDS structure parameters.

| Parameter	Unit	$E_1T = 14.5MV/m$	$E_1T = 8.5MV/m$
Operating frequency	MHz	1300.0	1300.0
Phase velocity	relative	1.0	1.0
Aperture diameter $2a$	mm	47.0	46.0
Total web thickness	mm	32.0	32.0
Gap length g	mm	73.464	66.162
Drift tube cone angle	deg.	20.0	20.0
Lower drift tube radius r_1	mm	8.87	2.25
Upper drift tube radius r_2	mm	8.87	2.42
Upper cell radius r_3	mm	8.50	8.50
Outer cell radius R_c	mm	85.45	82.52
Effective shunt impedance Z_e	$M\Omega/m$	33.15	37.76
Coupling coefficient k_c	%	9.1	11.4
Quality factor Q_0		21100	20700
Transit time factor T		0.783	0.801
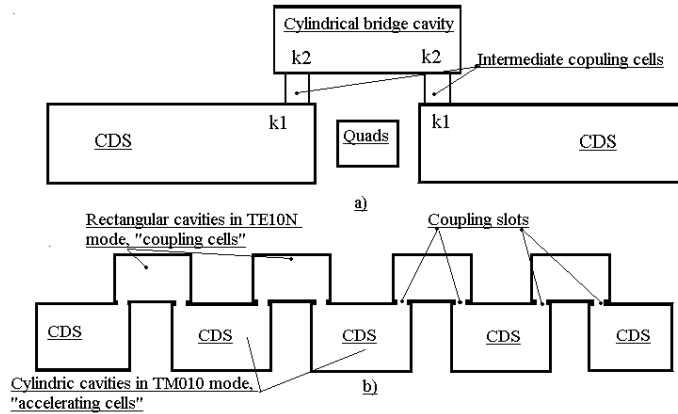
Figure 3.2.1: A sketch of the sections coupled by CBC (a) and RDCB (b).

Later, to solve the mode-mixing problem for CBS, a multi-cell CBS [6] was developed and tested at a high rf power level. Following the well known concept [5], a CBC is attached to the CDS section through the intermediate coupling cell (Fig.3.2.1a). In the chain of coupled cells, which describes the total cavity, a bridge cavity is equivalent to a modified accelerating cell which is displaced from the beam axis. In order to reduce the rf losses in the bridge cavity one should provide asymmetrical coupling in the intermediate cell $k_2 > k_1$. The tuning procedure for the CBC is evident due to the CBC design philosophy. As the result of comparison of different CBC types, the multi-cell bridge cavity [6] looks now like a preferable CBC solution.

Direct coupling. Another concept of coupling bridge cavities is possible [7] with Rectangular Directly Coupled Bridges (RDCBs). To illustrate the philosophy of RDCBs, let us consider a bi-periodic chain of coupled cavities (Fig.3.2.1b). The first type of cavities are cylindrical CDS sections, exited in the TM_{010} mode. The second type of cavities are rectangular ones, exited in the TE_{10n} mode. To simplify the manufacturing procedure for a rectangular cavity, let us choose transversal dimensions equal to those of standard waveguide WR650, recommended at operating frequency. With such a choice we automatically solve the mode-mixing problem for RDCBs, because the dimensions of the waveguide are defined for a single mode operation of the TE_{10} wave.

Both types of cavities are coupled through coupling slots, forming the chain of coupled cavities, in which cylindrical cavities are equivalent to accelerating cells, and rectangular cavities - to coupling ones. The coupling slots are placed to couple the H_ϕ component in the cylindrical cavity with H_x in the rectangular one. Let us define the mode in the rectangular cavity, for example TE_{10N}, and choose the length of the rectangular cavity in a such way as to have the frequency of this mode equal to the operating frequency of the accelerating cells. We get a usual chain of coupled cavities which is well known from the CCS description [5]. If one matches the frequencies of the accelerating mode (operating mode of the tank, really it is the frequency of CDS sections taking into account the effect of the coupling slots) and the coupling mode (the frequency of the rectangular cavity also taking into account the effect of the coupling slots), one will have an accelerating system, consisting of two types of cells, with a continuous dispersion curve. The central, operating mode is a $\pi/2$ mode, with a strong field in the accelerating (CDS) sections and a weak field in the coupling cells (RDCB) and with all properties of stabilization. One should take into consideration that for odd N the TE_{10N} mode has the H_x component of different signs at the ends of the bridge. In this case at the operating $\pi/2$ mode the phase shift between CDS sections is 2π. For even N the coupling coefficient k_c at the ends of RDCB has the same sign and the phase shift between CDS sections is π.

The evident question to be answered is - how can we match such directly coupled bridges with the driving waveguide, if there is no field in the bridge cavity at the operating mode? This statement is only the result of our analysis based on a single-mode approximation to describe RDCB. In the study of multi-mode approximation for the RDCB description, one will find a weak, but nonzero field in the bridges at the operating mode, sufficient to match with a driving waveguide. For odd N the field in RDCB at the operating $\pi/2$ mode can be represented as the sum over TE_{10n} modes with even n, for even N - with odd n.

RDCBs were proposed for high energy accelerating structures, tested at high rf power level with the Disk and Washer and Annular Coupled structures [8] and have successfully been operating in the main part of the Moscow Meson Facility linac for a long time.
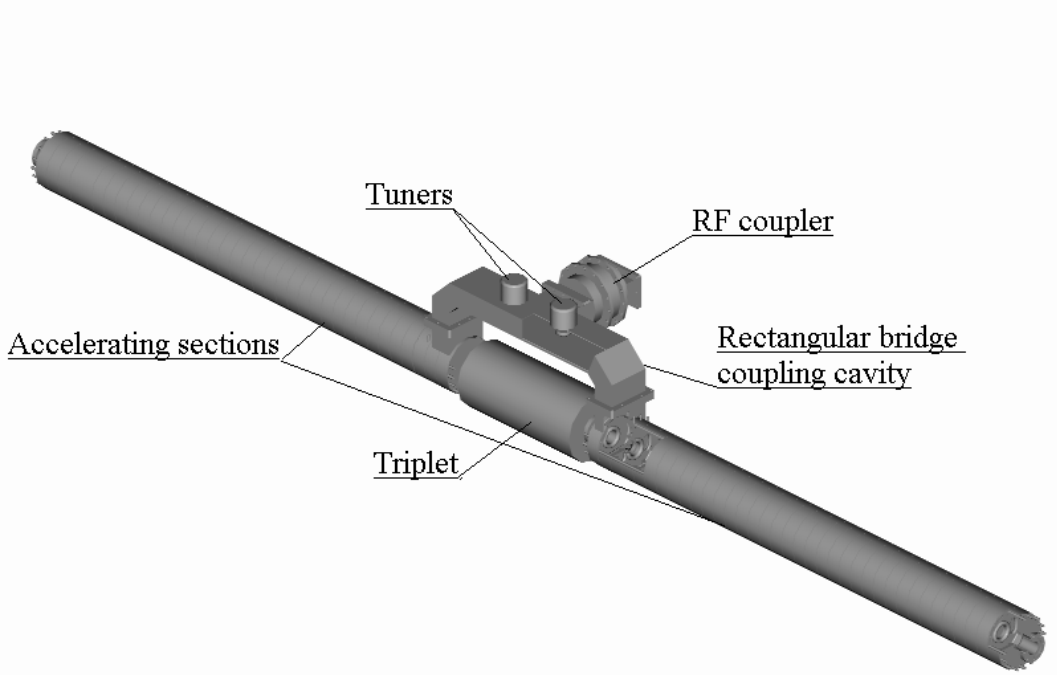
Figure 3.3.1: Accelerating cavity in the second PPA part.

3.3 Accelerating cavities for the second part of the PPA

Both well known Cylindrical Bridge Cavities and Rectangular Directly Coupled Bridges may be used in the accelerating cavities for the PPA second part. In comparison with CBCs with intermediate coupling cells RDCBs have:
- a better mode separation with smaller rf losses,
- a smaller transverse dimensions,
- a flexible tuning of the rf field between CDS sections,
- a simpler manufacturing and tuning procedure.

Due to the smaller transverse dimensions (and lower stored energy), an RDCB provides stronger coupling (with the same coupling slots dimensions) between CDS sections. It leads to a higher stability of AC parameters. To maintain features of the CDS structure as easy-to-do low-cost ones, Rectangular Directly Coupled Bridges (RDCB) look more preferable.

Let us consider two CDS sections coupled in the middle with an RDCB (Fig.3.3.1). Each CDS section has 19 accelerating cells with the design accelerating gradient $E_1 T \approx 8.5 MV/m$.

The distance between the centers for the end cells in the adjacent sections is $9\beta\lambda/2$ and the RDCB should provide a π phase shift between sections, so a TE_{10N} mode with even N should be chosen. It means that the RDCB length along the 'middle line' $L_s + 2H_l$ (see Fig.3.3.3) should be close to $N\Lambda/2 \approx L_s + 2H_l$, where $\Lambda \approx 32.221 cm$ is the wavelength of the TE_{10} wave in the WR650 waveguide. To combine the requirements to the distance between the sections $L_s = 9\beta\lambda$ and the total length of the bridge coupler to be $L_s + 2H_l \approx$

16

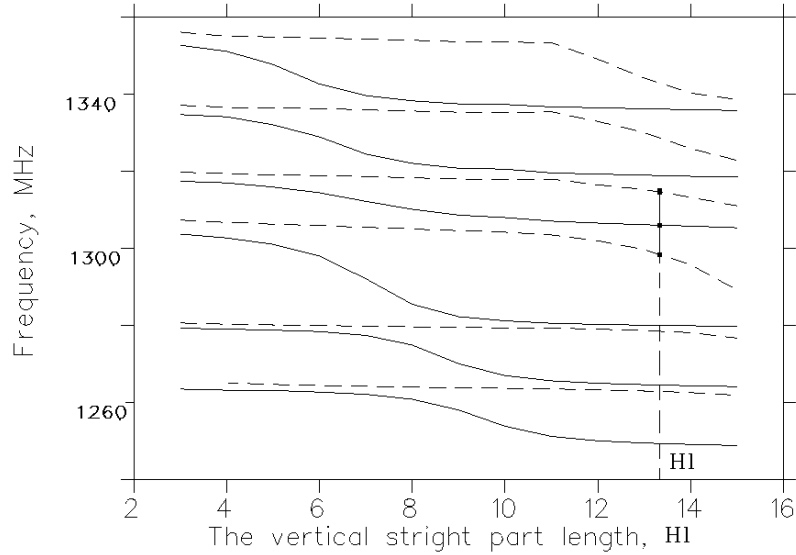Figure 3.3.2: The AC mode frequencies dependences on the RDCB vertical part length.
Solid lines - even modes, dashed lines odd modes.

$N\Lambda/2$, the RDCB should be formed in Π-shape.

Changing the RDCB length L_s+2H_l, one can change a mode frequencies in a total (RDCB +2CDS sections) cavity. The dependences of the mode frequencies on the vertical RDCB part length H_l are plotted in (Fig. 3.3.2), because the length L_s along the beam axis if fixed $L_s \approx 9\beta\lambda$. The plots on (Fig. 3.3.2) show a typical behaviour for coupled systems. Due to the π phase shift between CDS sections, the operating mode should have an even symmetry for E_z with respect to the cavity middle-plane. In this case neighbour modes will have odd symmetry. The correct value of the vertical part length H_l should be chosen so that the dependence $f_0(H_l)$ has a small slope and neighbour modes are placed symmetrically at the frequency scale.

As one can see in (Fig. 3.3.2), the value $H_l \approx 13.5cm$ is the correct one. In this case at the operating mode there is a strong field in the sections (Fig. 3.3.3) and relatevily low field in the RDCB. The coupling cavity doesn't increase rf losses essentially (low field in RDCB) but can be matched with the driving waveguide (field in RDCB is low, but nonzero). Symmetrical placement of nearest neighbour modes provides a high field distribution stability in the total cavity. As it is evident, if the value $H_l \approx 13.5cm$ is unsufficient due to the mechanical design, a new value $H_l + \Lambda/2$ may be chosen also.

To tune the cavity parameters, the RDCB is equipped with two plug tuners (Fig.3.3.1). With simultaneous motion of the RDCB tuners we can change the own frequency of the RDCB, thus tuning the position of the nearest modes practically with small changes of the operating frequency for the total cavity. With opposite motion of the RDCB tuners one can change the rf field level between CDS sections by several percent. For even N the driving waveguide is attached to the narrow wall in the RDCB middle point, matching the H_x component of the TE_{10} wave in the WR650 waveguide with the H_z component of
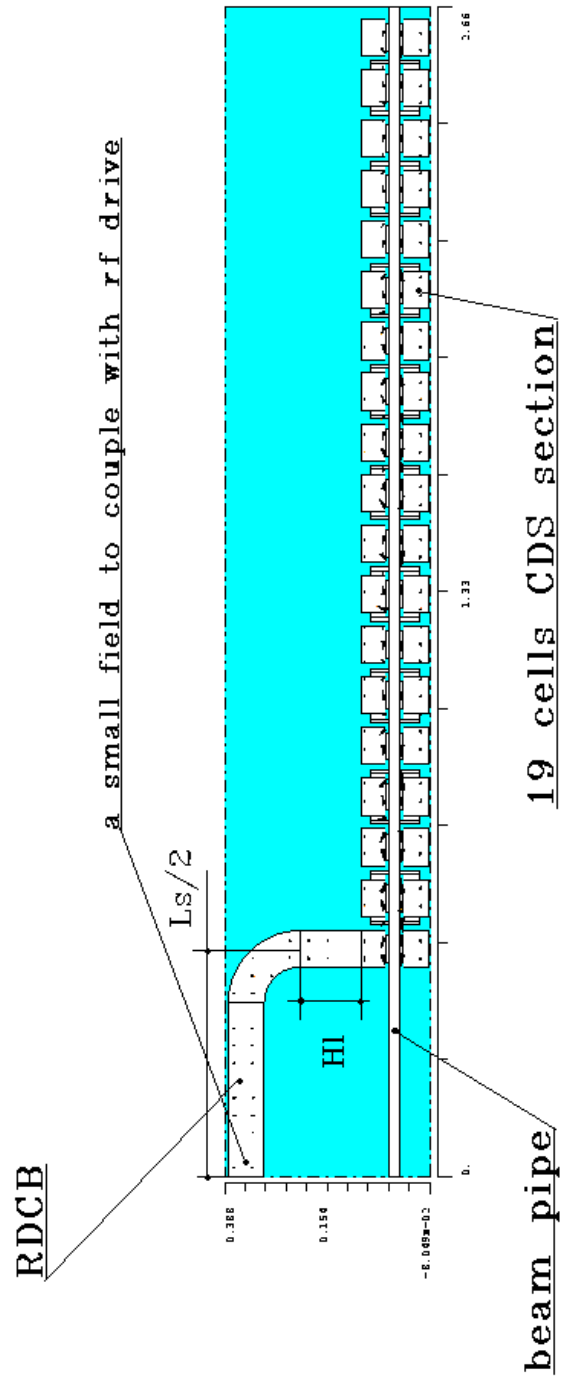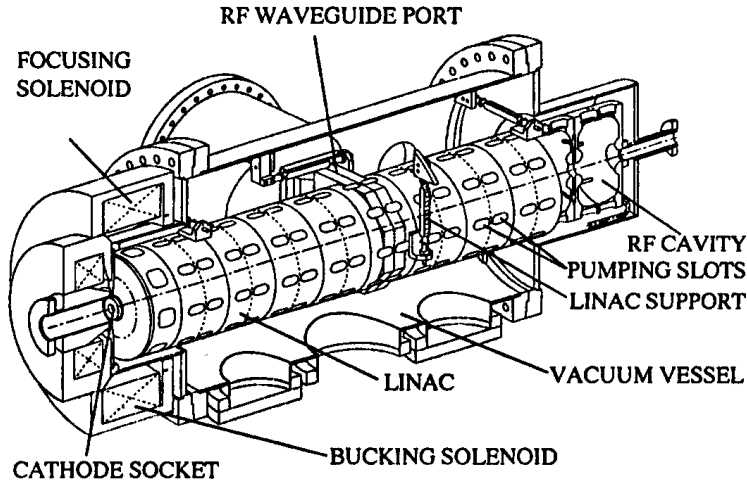
17

Figure 3.3.3: Electric field distribution for the operating mode.

the TE_{10N} RDCB mode.

RF WAVEGUIDE PORT

FOCUSING
SOLENOID

RF CAVITY
PUMPING SLOTS
LINAC SUPPORT

VACUUM VESSEL

LINAC

CATHODE SOCKET

BUCKING SOLENOID

AFEL linac schematic. The focusing solenoid provides compensation of space-charged induced emittance growth. The Bucking Solenoid is adjusted to give zero field at the surface of the cathode. The LINAC is an eleven-cell pi/2-mode structure. The LINAC can be operated from 77K to greater than 400K. The support structures allow only rotation of the accelerator on cool-down, not translation.

Figure 3.4.1: A schematic sketch of AFEL accelerator.

3.4 RF power system

To reduce the total linac cost and to simplify maintenance the PPA rf system is supposed to be based on the standard powerful TESLA equipment [1] - the same $10MW$ klystron with two waveguide outputs, the powerful circulators after the klystron output windows, the anode modulator and the standard WR650 waveguide as Transmission Line (TL). But the PPA rf system should take into account the PPA particularities. Contrary to the regular TESLA rf system, in the PPA each klystron feeds only one normal conducting Accelerating Cavity (AC). We assume here the design of the L-band rf power combiner to be done and the PPA ACs have a single rf input coupler. A total rf power of $\approx 10MW$ in a single waveguide WR650 is rather high, but there is the experience of the L-band AFEL linac [9] - single rf input (Fig. 3.4.1), $17MW$ klystron, $30\mu s$ rf pulse, repetition rate up to 100 Hz.

3.5 A special shape of the rf pulse beginning.

During the main part of the rf pulse $10MW$ of rf power through a single WR650 waveguide is acceptable. The power limit of this waveguide for stable operation is $P_{crit} \approx 14MW$ [1]. But in the rf pulse beginning the reflection from the cavity takes place. If the driving rf pulse has a simple rectangular shape,

$$E^{dr}(t) = \begin{cases} 0 & 0 > t, t > t_{rf} \\ E^{dr}_{nom} & 0 \le t \le t_{rf}, \end{cases}$$

where t_{rf} is the rf pulse duration, the reflected wave amplitude $E^{ref}(t)$ can easily be found as:

$$E^{ref}(t) = \mathcal{L}^{-1}(\mathcal{L}(E^{dr}(t))F_{rc}(p)), \qquad (5)$$

where $\mathcal{L}()$ and $\mathcal{L}^{-1}()$ are direct and inverse Laplace transformation operators, $F_{rc}(p)$ is the transformation of the cavity response. In the general case of a slightly detuned single mode cavity $F_{rc}(p)$ is [10]:

$$F_{rc}(p) = \frac{\eta - 1 - \tau_l \eta(1 + \eta)(i\Delta\omega + p)}{\eta + 1 + \tau_l \eta(1 + \eta)(i\Delta\omega + p)}, \qquad (6)$$

where ω_0 is the operating frequency, $\Delta\omega = \omega_0 - \omega_1, \mid \Delta\omega \mid \ll (\omega_1, \omega_0), \omega_1$ is the cavity resonant frequency, and η is the coupling coefficient between the cavity and the waveguide. The loaded quality factor Q_l and the rise-time constant τ_l are defined with η as:

$$Q_l = \frac{Q_0}{1 + \eta}, \qquad \tau_l = \frac{Q_0}{\omega_0(1 + \eta)}, \qquad (7)$$

where Q_0 is the quality factor of the unloaded cavity. The time dependence for the reflected wave amplitude is:

$$E^{ref}(t) = E^{dr}_{nom} \frac{2\eta \exp(-\frac{t}{\tau_l} - i\Delta\omega t) + \eta - 1 - i\Delta\omega(1 + \eta)\tau_l}{\eta + 1 + i\Delta\omega(1 + \eta)\tau_l} = E^{dr}_{nom}(b(t) + b_0) \qquad (8)$$

At the first moments $t \approx 0$ the reflected wave amplitude $E^{ref}(t)$ is comparable with the forward one E^{dr}_{nom} ($b(0) \approx 1$, b_0 is the reflection due to cavity mismatch and usually is $b_0 \ll 1$). In the waveguide there will be regions where two waves add. If E^{dr}_{nom} corresponds the to nominal rf power $P_{nom} = 10MW$, the maximal amplitude of the field possible in the waveguide is $E^{dr}_{nom} + E^{ref} \approx 2E^{dr}_{nom}$, corresponding to rf power $P_{max} \sim (2E^{dr}_{nom})^2 \sim 4P_{nom} = 40MW$. It exceeds the safety limit for the WR650 waveguide with air filling.

Due to the low - as compared to a superconducting structure - Q_0-factor (≈ 23000), the field rise-time for the PPA AC is quite short $3\tau_l \approx 7.5\mu s$. The rf pulse with $\approx (815 \div 820)\mu s$ duration is sufficient for the PPA purpose and the standard TESLA modulator can be modified to reduce the pulse length.

The enlarged reflection and overvoltage in the TL occur during a rather short transient period $3\tau_l \approx 7.5\mu s$, which is small in comparison with the total pulse length $\approx 820\mu s$. If overvoltage is a serious problem, we can reduce it by a special shape of the rf pulse beginning. The cavity becomes saturated with the forward wave from the rf source $E^{dr}(t) \exp(i w_0 t)$. Starting with the reduced driving amplitude in the beginning of the rf pulse, we will shorten the reflected wave amplitude and significantly diminish the overvoltage. Then the forward wave amplitude will be increased to a nominal value, but the reflected wave amplitude during increasing will be smaller than for a simple step-like rf pulse beginning.

Let the driving rf pulse envelope $E^{dr}(t)$ be described as:

$$E^{dr}(t) = \begin{cases} E^{dr}_{beg}(t) \le E^{dr}_{nom} & t \le t_b \\ E^{dr}_{nom} & t_b \le t \le t_{rf} \end{cases}$$

where t_b is a time duration for the special pulse shape beginning. Different approaches are possible.

One can try different functions for the E_{beg}^{dr} description, find the reflected wave amplitude by using (6) and estimate the overvoltage $E^{ov}(t) = E^{dr}(t) + E^{ref}(t)$.

Generally, the inverse problem can be solved. Let us define the overvoltage needed $E^{ov}(t) = E^{dr}(t) + E^{ref}(t)$ reasonable for the safe operation. Then one can do:

$$E^{ov}(p) = \mathcal{L}(E^{ov}(t)) = E^{dr}(p) + E^{ref}(p) = E^{dr}(p) + E^{dr}(p)F_{rc}(p) = E^{dr}(p)(1 + F_{rc}(p)), \quad (9)$$

$$E^{dr}(t) = \mathcal{L}^{-1}\left(\frac{E^{ov}(p)}{1 + F_{rc}(p)}\right) \quad (10)$$

In this way only one limitation exists - not all shapes for $E^{ov}(t)$ have a physical meaning and will the shape $E^{dr}(t)$ be technically reasonable?

Let us consider another algorithm, more suitable for modern rf systems with digital control. It means that the rf control system has small, but finite time steps of discretization t_d to represent any signal. During this time step every signal is assumed as constant value. Let us describe the control signal for E^{dr} as a sum of several steps:

$$E^{dr}(t) = E_{nom}^{dr} \sum_{n=1}^{N} a_n h(t - (n-1)t_d), \qquad a_n \leq 1.0, \quad (11)$$

where $h(t) = 0, t < 0, h(t) = 1.0, t \geq 0$ is a usual step function. The amplitude at the first step a_1 is determined as:

$$a_1 = \left(\frac{P_{crit}}{4P_{nom}}\right)^{1/2} \quad (12)$$

With such a choice we limit the overvoltage in the waveguide by the equivalent power P_{crit} at the moment $t = 0$. Then the reflected wave from the first step will decrease and to the beginning of the second step $t = t_d$ will be $E_{nom}^{dr} a_1 \exp(\frac{-t_d}{\tau_l})$. The second step amplitude a_2 can be derived from the equation:

$$a_1\left(1 + \exp(\frac{-t_d}{\tau_l})\right) + 2a_2 = 2a_1, \qquad a_2 = 0.5a_1\left(1 - e^{\frac{-t_d}{\tau_l}}\right), \quad (13)$$

In the beginning of the second step the overvoltage will be returned to the equivalent value P_{crit}, decreasing during this step. In this equation, and further, we assume the tuned ($\Delta\omega = 0$), perfectly matched ($\eta = 1.0$) cavity. The general case may be considered by using (8). We also neglect the delay in the waveguide. To consider this delay time, one should artificially (in consideration) increase t_d.

Following the general idea - to keep in the beginning of each step the total overvoltage equivalent to P_{crit}, for the a_{n+1} step amplitude one finds (defining $x = \exp(\frac{-t_d}{\tau_l})$):

$$a_1(1 + x^n) + a_2(1 + x^{n-1}) + ... + a_k(1 + x^{(n-k+1)}) + ... + a_n(1 + x) + 2a_{n+1} = 2a_1. \quad (14)$$

Comparing equations for a_n and a_{n+1} determination, we get:

$$a_{n+1} = 0.5a_n\left(1 + \exp(\frac{-t_d}{\tau_l})\right). \quad (15)$$

The procedure should be finished with N if $\sum_{n=1}^{N} a_n \geq 1.0$ and the last step may be reduced to have $E^{dr}(t = Nt_d) = E_{nom}^{dr}$ value. This procedure converges allways if $P_{crit} > P_{nom}$.

But it is a condition for the stable operation during the total rf pulse. Developed in terms of voltage, the $E^{dr}(t)$ dependence can easily be translated into an rf power expression $P_{dr}(t)$ by using the relation $P \sim E^2$.

The number of steps N depends on P_{crit}/P_{nom} and t_d/τ_l. For different P_{crit}/P_{nom} ratios the forward and reflected waves, the overvoltage and the cavity voltage are plotted in (Fig. 3.5.1) in terms of rf power (Fig. 3.5.1a-c) and in terms of voltage (Fig. 3.5.1d) for $t_d = 1\mu s, Q_0 = 24000, \tau_l = 2.938\mu s, P_{crit} = 14.0MW$. The total length of the pulse beginning $t_b = t_d(N-1)$ mainly depends on the P_{crit}/P_{nom} ratio. Assuming $P_{crit} = 14MW$, for $P_{nom} = 5MW$ only two additional steps are necessary, eight for $P_{nom} = 10MW$ and twenty one for $P_{nom} = 13.5MW$. But the total duration of the transient processes increases not so strongly. The total transient processes consist of a special pulse beginning and a natural tail. With low P_{nom} value one has a very short pulse beginning and a long natural tail. During the pulse beginning the rf power comes into the cavity and to the end of the pulse beginning reaches the P_{st} value. With P_{nom} increasing or P_{crit}/P_{nom} decreasing more steps are necessary, but P_{st} becomes relatively higher, the natural tail begins from a higher value of the cavity voltage and takes smaller time. Comparing the plots in (Fig. 3.5.1a) and (Fig. 3.5.1c) one sees practically the same finish of the transient during time $\approx 25\mu s$ in spite of the fact that the beginning takes place $2\mu s$ and $8\mu s$, respectively.

With $t_d \to 0$ we will find a smooth function $E^{dr}(t)$. The same as in (Fig. 3.5.1) graphs are plotted in (Fig. 3.5.2) for $t_d = 0.01\mu s$. Comparing the plots in (Fig. 3.5.1) and (Fig. 3.5.2) one sees smoothing of the 'saw-tooth' behavior for overvoltage, forward and reflected power. The dependence of the cavity voltage practically doesn't change. The time duration of the pulse beginning slightly decreases because we pump the cavity more effectively. One can check directly, by using (10), that the function

$$E^{dr}(t) = \begin{cases} E_{nom}^{dr}\left(\frac{P_{crit}}{P_{nom}}\right)^{\frac{1}{2}}\left(1 - 0.5\exp\left(-\frac{t}{2\tau_l}\right)\right) & 0 \le t \le t_b \\ E_{nom}^{dr} & t_b \le t \le t_{rf} \end{cases}$$

where

$$t_b = 2\tau_l \ln[2 - 2(\frac{P_{nom}}{P_{crit}})^{\frac{1}{2}}], \tag{16}$$

is a continuous one for $E^{dr}(t)$ approximation (Fig. 3.5.1), leading to the optimal overvoltage time dependence

$$E^{ov}(t) = \begin{cases} E_{nom}^{dr}\left(\frac{P_{crit}}{P_{nom}}\right)^{\frac{1}{2}} & 0 \le t \le t_b \\ E_{nom}^{dr}\left(\left(\frac{P_{crit}}{P_{nom}}\right)^{\frac{1}{2}} - 1\right)\exp\left(-\frac{t-t_b}{\tau_l}\right) + E_{nom}^{dr} & t_b \le t \le t_{rf} \end{cases}$$

With such approximation for the rf pulse beginning we keep the overvoltage constant during the period $0 \le t \le t_b$ as much as possible, providing the most effective cavity excitation, then release the transient process and the overvoltage decreases by the natural exponential law to the normal operating value E_{nom}^{dr}.

To use the procedure proposed one only should specify the tolerable overvoltage E^{ov}. For the end of the pulse such a procedure is not necessary, because there is no forward wave and the reflected wave can't be higher than the forward one. The procedure proposed does not protect against overvoltage if sparking in the accelerating cavity takes place during the rf pulse. But sparking in the AC is not an ordinary situation, will cause an interlock event and should be removed during cavity rf conditioning.
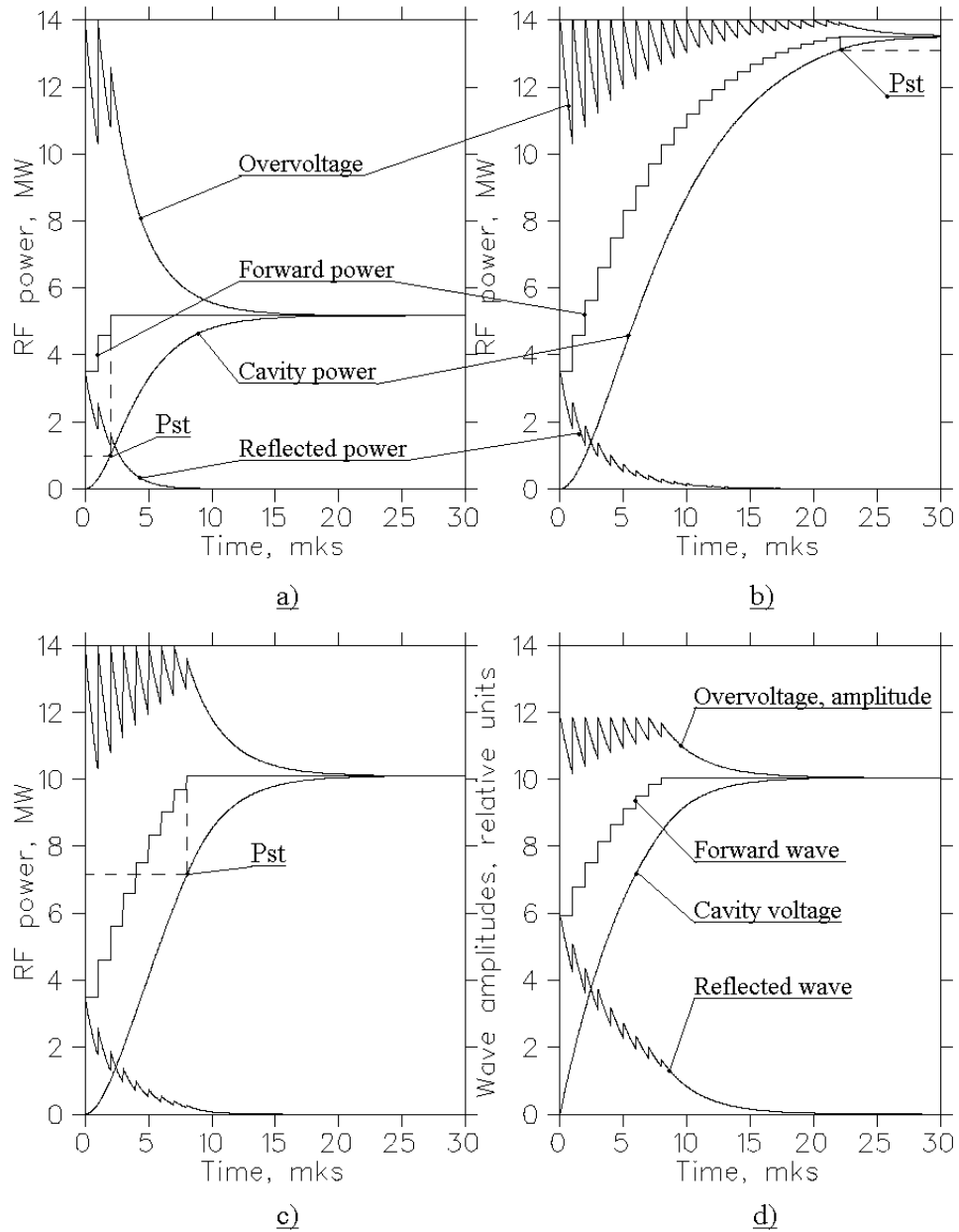
Figure 3.5.1: The plots of transients in the NC cavity for the the sum of step-like control signals, a)-c) - rf power, d) - rf voltage. $t_d = 1\mu s, \tau_l = 2.938\mu s, P_{crit} = 14.0MW$. a) - $P_{nom} = 5.0MW$, b) - $P_{nom} = 13.5MW$, c),d) - $P_{nom} = 10.0MW$.
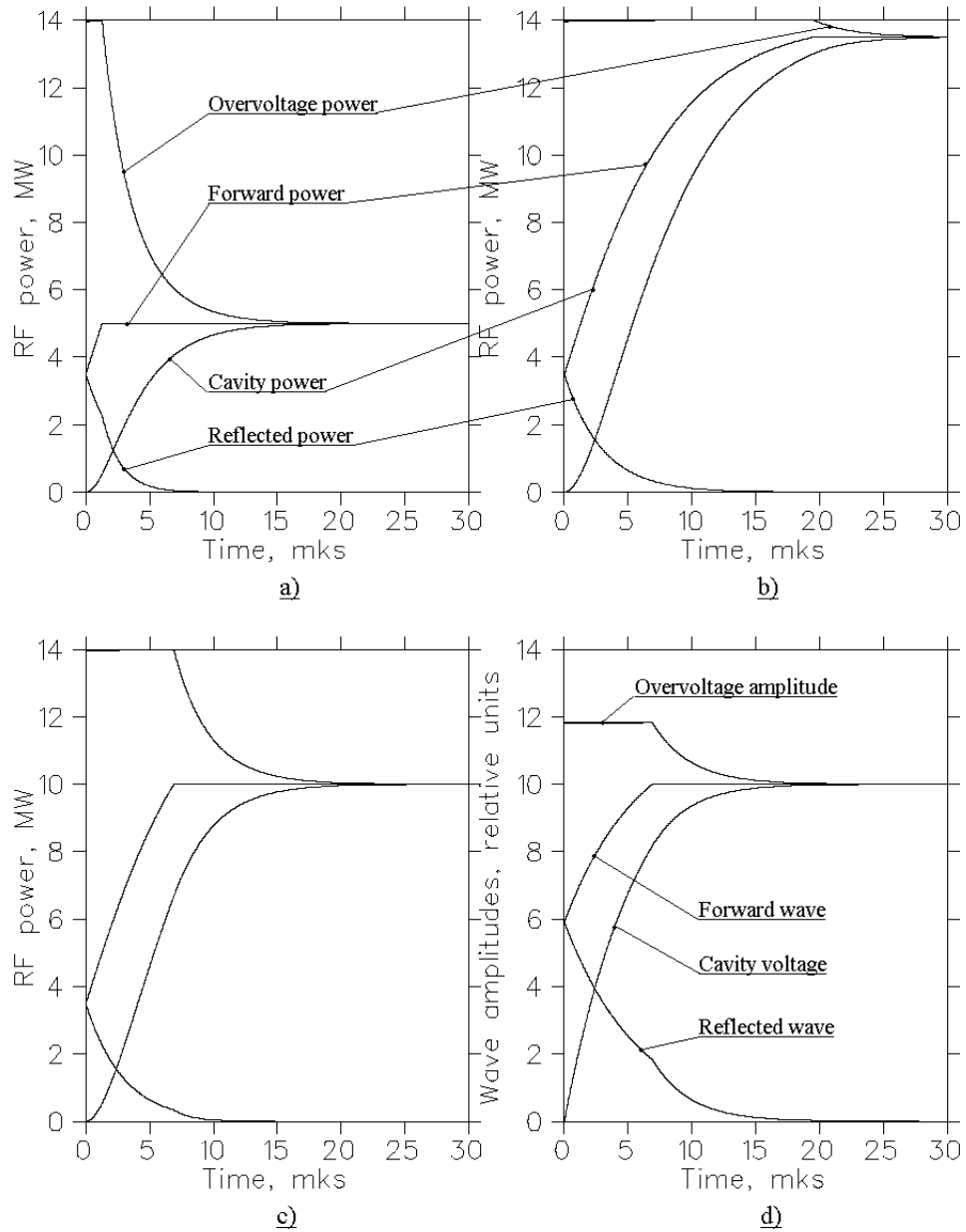
24

Figure 3.5.2: The plots of transients for a smooth control signal. a)-c) - rf power, d) - rf voltage. $t_d \to 0, \tau_l = 2.938 \mu s, P_{crit} = 14.0 MW$. a) - $P_{nom} = 5.0 MW$, b) - $P_{nom} = 13.5 MW$, c),d) - $P_{nom} = 10.0 MW$.
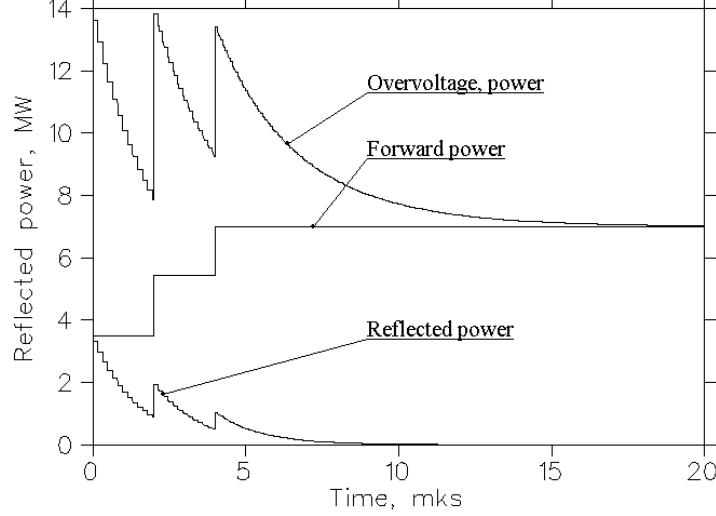
Figure 3.5.3: The plots of transients for a multi-cell AC.
$t_d = 2\mu s, \tau_{tr} = 163ns, P_{crit} = 14.0MW, P_{nom} = 7.0MW$.

3.6 Transients in a multi-cell cavity

In comparison with a single cavity, the transient in multi-cell accelerating cavities has some particularities related with a travelling wave propagation along the cavity from the rf input point to the cavity end-wall and back. Supposing the rf input being in the middle of the cavity, the time τ_{tr} for the wave propagation for a long PPA AC is:

$$\tau_{tr} = \frac{2L}{c\beta_g}, \qquad \beta_g = \frac{\pi k_c}{4} \approx 0.09, \qquad \tau_{tr} \approx 160ns, \qquad (17)$$

where k_c is the CDS coupling coefficient, c is the velocity of light, $L = \frac{N_c\beta\lambda}{2} = \frac{19\lambda}{2} \approx 2.2m$. The travelling wave attenuation constant α is also important for the transient description:

$$2\alpha L = \frac{\tau_{tr}}{4\tau_l} = \frac{2N_c}{k_c Q_0} \approx 0.123Np, \qquad N_c = 19. \qquad (18)$$

The transient effect in the multi-cell cavity can be considered as a summation of travelling waves propagation. A general theory of transients in multi-cell AC has been developed in [10]. For a step-like driving rf signal with E_{nom}^{dr} amplitude the reflected wave amplitude is:

$$E^{ref}(t) = E_{nom}^{dr}(\xi\frac{1 - (\eta\xi)^{[\frac{t}{\tau_{tr}}]} - \eta + \eta(\eta\xi)^{[\frac{t}{\tau_{tr}}]+1}}{1 - \eta\xi}), \qquad \xi = \exp(-i\tau_{tr}\Delta\omega - 2\alpha L), \quad (19)$$

where $[\frac{t}{\tau_{tr}}]$ is the integer part of the $\frac{t}{\tau_{tr}}$ ratio. For the tuned ($\Delta\omega = 0$) and perfectly matched cavity (for multi-cell cavities a condition of critical coupling is $\eta = \exp(-2\alpha L)$) relation (19) simplifies:

$$E^{ref}(t) = E_{nom}^{dr}\eta^{2[\frac{t}{\tau_{tr}}]+1}. \qquad (20)$$

26

In spite of the fact that we for the transient description in the a multi-cell cavity we don't use the quality factor Q_0 or rise-time τ_l, the envelopes for reflected wave and cavity voltage exhibit the same behavior as for a single cavity, with the exponential law $\exp(-\frac{t}{\tau_l})$. But these envelopes are modulated by steps with time duration τ_{tr}. Such a transient effect particularity was observed for multi-cell cavities in precise experiments [10]. Because the general behavior of the transient effects for multi-cell cavity is the same as for a single one, we can apply the procedure of the overvoltage decreasing with the same result. For example, in (Fig. 3.5.3) the dependencies for overvoltage, reflected and forward power are plotted for multi-cell AC assuming three steps in the rf pulse beginning.

The important point of the transients in the multi-cell AC is the field strength in the coupling cells. During the time $0 \leq t \leq t_{tr}$ the first travelling wave propagates from the rf input to the cavity end and back. During this time in the cavity there exist coupling cells only with a direct propagating wave and the electric field in this case has a maximal value. With reflected (from the cavity end wall) waves the field in coupling cells will be decreased. In compensated accelerating structures the travelling is composed as $E_{tr} = E_a + iE_c$ - a field of accelerating E_a and coupling E_c modes, normalized with a condition $\int_v E_a^2 dV = \int_v E_c^2 dV$. As compared with accelerating cells, coupling cells usually have a much less volume (and a higher field strength at the equal stored energy). Moreover, in accelerating cells a maximum electric field on the surface is a point for consideration. If sparking in coupling cells is possible, the best condition is during the time interval $0 \leq t \leq t_{dr}$. If the accelerating gradient design value is E_0T, during the first transient in accelerating cells the field $E_a^1 = E_0T2\alpha L$ [10] and the stored energy W_c^1 in a coupling cell is:

$$W_c^1 = \frac{N_c^2(E_0T)^2\beta c}{\pi Z_e f_0^2 k_c^2 Q_a}. \tag{21}$$

The corresponding value E_c^1 should be considered during the structure design. For the PPA CDS (both options, see Chapter 3.1) $E_c^1 \leq 0.5E_k$, where E_k is the Kilpatrick sparking threshold.

3.7   Summary

The PPA accelerating structure parameters have been revised taking into account a reasonable PPA acceptance reduction and a single rf input rf power system. The aperture diameter is decreased to 46 mm, leading to an improvement of the accelerating structure parameters. The coupling bridge cavities combine two accelerating sections in a joint resonant system. To maintain features of the CDS structure effective, easy-to-do and low-cost, Rectangular Directly Coupled Bridges are recommended.

The single point rf input option for the PPA rf system is an attractive choice, leading to simpler control systems, reasonable requirements to the transmission line and accelerating structure. The special shape for the rf pulse beginning is proposed to reduce the overvoltage in the transmission line. The procedure for the overvoltage limitation can be applied both for single and multi-cell cavities. The transient time increasing is of the order of several microseconds and negligible in comparison with the total rf pulse duration.

4 Study of the magnetic insertion for the PPA.

A magnetic insertion at a beam energy of $\sim 100\,\mathrm{MeV}$ is an essential PPA part [2]. Its main purpose is to separate the positrons from the electrons and photons after the first stage of acceleration. Additionally it serves to ensure a parallel raising of the beam to a height of $\sim (1.0 \div 1.2)\,\mathrm{m}$ and positron beam collimation both in transverse phase space and momentum spectrum. To serve this purpose a special four cells magnetic insertion scheme was proposed [2]. The detailed description of the insertion magnetic structure has been done in paper [2]. Briefly it consists of several parts and can be presented schematically as the following chain: $M_1 - S^+ - S^- - S^+ - S^- - M_2$. Here S is the mark of the unit cell which is composed of a dipole and two quadrupoles in front of it and behind it. The $S-$sign means a sign of the magnetic field in the dipole. M_1 and M_2 are 4-quadrupole matching sections. In the previous studies [2] this magnetic structure has shown the general properties to satisfy the purposes mentioned above.

The design and study of this system were carried out by using the first order matrix formalism.

The goal of the present study is to estimate the influence of the nonlinear effects on the particle dynamics and beam quality during the tracing throught the insertion magnetic structure. To solve this problem a special branch TrackFMN of the computer code FMN [12] was developed. For 6-dimensional tracking of noninteracting particles by TrackFMN using the next options are currently availiable :

- the Hamiltonian of dipole magnets contains all term up to 3rd order with respect to coupled synchro-betatron oscillations. For drifts, collimators, quadrupoles and solenoids the unexpanded Hamiltonian is used. Besides there are high order terms for octupoles and other multipoles;

- for all elements in the beam line the Hamiltonian contains all term up to 3rd order with respect to coupled synchro-betatron oscillations for a simulation of the orbital motion. Besides there are higher order terms for octupoles and other multipoles;

- as compared to previous item, the Hamiltonian contains only all terms up to second orders in coupling between transverse and longitudinal motion.

To estimate the positron transmission through the system, the following criteria were introduced:

$$\text{the maximum part of the particle} \quad \eta$$
$$\text{containing in phase space with dimensions}$$
$$\frac{\Delta W}{W_c} = 30\,\% \quad ; \quad W_c \in [90 \div 120]\,\mathrm{MeV} \tag{22}$$
$$\Delta\varphi = 15^\circ$$
$$\varepsilon_x \le 0.036\,\mathrm{m} \quad ; \quad \varepsilon_y \le 0.036\,\mathrm{m} \quad ; \quad \varepsilon_x + \varepsilon_y \le 0.048\,\mathrm{m},$$

where W_c - is the system central energy, ΔW - is the acceptable energy interval, $\Delta\varphi$ - is the acceptable longitudinal interval calculated with respect to the basic length λ_{rf}, ε_x, ε_y - are the transverse beam emittances.

The results of simulations are listed in Table 4.1. It should be pointed out here that the results are presented for the optimum system central energy which is slightly varied for different nonlinear tracking conditions. For Tracking ♯2 the influence of the chromatic effects was switched off. It means that we only have the nonlinear effects of the beam geometry which essentially doesn't reduce the positron transmission. However the results

Table 4.1: Positron beam transmission results.

N	Method	Conditions	η, %
1	Linear tracking		25.6
2	Nonlinear tracking	Chromaticity off	20.3
3		Chromaticity on	3.3
4		Matching improvements	3.8
5		Separated chromatic correction	4.2
6		Combined chromatic correction	6.3

Table 4.2: Different partial chromaticities Q'_x/Q'_y.

N	M_1	S^+	S^-	S^+	S^-	M_2	Σ
3	1.59/2.56	0.73/1.35	0.73/1.35	0.73/1.35	0.73/1.35	4.40/1.52	8.91/9.48
4	0.46/0.86	0.10/0.90	0.73/1.35	0.73/1.35	0.63/0.40	1.33/0.78	3.91/5.64
5	0.46/0.86	0.19/0.78	0.80/1.30	0.66/1.27	0.62/0.36	1.33/0.78	4.06/5.35
6	0.46/0.86	0.02/0.67	0.50/1.03	0.75/1.06	0.75/0.31	1.33/0.78	3.81/4.71

of Tracking ♯3 show a drastic drop of the positron beam transmission quality caused by the nonlinear chromatic effects. It can be concluded that the chromatic effects strongly dominate for the particle tracing at the relatively low energies.

To suppress the influence of the nonlinear chromatic effects, it was decided to estimate the chromatic contribution of the different magnetic parts by the well known parameter [13]:

$$Q' = -\frac{1}{4\pi} \int\limits_0^L \beta(s) \left\{ K_0(s) - D_x(s) K_0'(s) \right\} ds, \tag{23}$$

where $\beta(s)$ - is the betatron envelope function, $D_x(s)$ - is the dispersion function, $K_0(s) = \frac{e}{p_0}\frac{\partial B}{\partial x}$ - is the quadrupole strength parameter, $K_0'(s) = \frac{e}{p_0}\frac{\partial^2 B}{\partial x^2}$ - is the sextupole gradient parameter, e - is the positron charge, p_0 - is the system central momentum, s - is the longitudinal coordinate, L - is the system total length.

Instead of the standard way using (23) for the total circular accelerator, the formula (23) of chromaticity Q' is applied here to separate straight parts with quadrupoles for an arbitrary magnetic system. In Table 4.2 Tracking ♯3 corresponds to the magnetic system described in [2] and mentioned above. Further the tracking number from Table 4.2 is adequate to the one from Table 4.1. and the vertical y-plane is used as bending plane.

The following changes were introduced and studied:

Tracking ♯4. The matching sections M_1 and M_2 were modified to minimize their local chromaticities. Moreover from the fist S^+ and last S^- cells two quadrupoles were removed in front of the dipole and behind it, respectively.

Tracking ♯5. The separated sextupoles with a length of 15 cm were placed between elements of the bending part. The total number of sextupoles is 15.

Tracking ♯6. In each quadrupole of the bending part the combined sextupole was placed.

  From the data analysis the following conclusions can be made:

- the chromatic nonlinear effects are dominant for determining the particle dynamics inside the magnetic insertion and the beam quality at the separator output;

- the separated sextupole correction is not effective because the magnetic system has an

evident FODO structure with small inter element spaces. That results in an inappropriate sextupole location between the system elements.

- apparently, the combined quadrupole-sextupole functions cannot essentially change the final results.

Moreover, the estimation of the beam tracking for an average energy of $\sim 280\,\mathrm{MeV}$, supposing the insertion at the PPA exit, doesn't lead to a significant improvement of the results.

Taking into account the role of the nonlinear chromatic effects, some simple reccomendations can be done to transport the beam with a high momentum spread:

4.1r - to use as few magnetic elements as possible;

4.2r - according to equation (23), to reduce the product $\beta(s)K_0(s)$ for the magnetic structure;

4.3r - to suppress the dispersion $D_y(s)$ to keep a small beam size inside the elements of the magnetic structure;

4.4r - to reduce the relative beam momentum spread by using the magnetic insertion at higher average beam energies.

The magnetic insertion [2] was designed in accordance with another requirement, i.e longitudinal beam collimation, especially in contradiction with (4.3r). The present study shows insuffcient beam transmission taking into account the nonlinear effects.

To improve the beam transmission and realize these principles an achromat bending scheme was investigated [14]. In this case the total magnetic insertion line can be presented as $(M_1 - SA - M_2)$, where M_1 and M_2 are the mentioned above 4-quadrupole matching sections, SA - is an achromat bending system consisting of two dipoles and a set of quadrupoles between them. The following requirements to the SA-design were fulfiled:

- the achromat bending system is arranged symmetrically with respect to the middle plane;

- to keep the value of dispersion function small two quadrupoles focusing in the bend plane are located as close to the dipoles as possible;

- a quadrupole defocusing in the bend plane is placed in the middle of the system.

Two different schemes for SA realization were designed and studied. The first one can be schematically described as $D^+ - F - D - F - D^-$ (Scheme$\sharp$1) and the second one - as $D^+ - FDF - D - FDF - D^-$ (Scheme$\sharp$2). Here D^+ and D^- are the dipoles with different field orientations; F and D are in the bend plane focusing and defocusing quadrupoles. In Table 4.3 the most typical parameters are listed for both schemes. The results are presented for bending in the vertical y-plane with characteristics acceptable for the PPA operation. As far as the main parameters are concerned, the Scheme$\sharp$1 and Scheme$\sharp$2 seen more or less adequate. Unfortunately for Scheme$\sharp$1 it is impossible to realize the acceptable matching with the PPA accelerating parts. Whereas for Scheme$\sharp$2 the parameters of the matching sections are satisfactory.

Scheme$\sharp$2 is proposed as a basic solution. For this case the acceptable positron transmission after the total magnetic insertion (taking into account AMD - first PPA parts) is 21.8 % for the system central energy 114.1 MeV for condition (22). Combining the sextupole correction with quadrupoles the total transmission can be slightly increased, but it leads to additional construction difficulties for quadrupoles and can be settled at the final stage of the design project. Structure functions of the magnetic insertion system are presented in (Fig. 4.1). In (Fig.4.2) and (Fig.4.3) there are phase space projections

Table 4.3. Characteristic pararameters for different magnetic insertion schemes.

| Parameter	Scheme ♯1	Scheme ♯2
Length, m	4.23	7.04
Bend angle, deg	18	11
Central energy, MeV	114.1	114.1
Maximum dispersion, m	0.241	0.154
Maximum β_x-function, m	2.79	2.39
Maximum β_y-function, m	5.23	3.72
Linear lengthening coefficient	-0.0245	-0.0091
Chromaticity Q'_x	0.58	0.74
Chromaticity Q'_y	1.00	1.01
Number of quadrupoles	3	7
Number of dipoles	2	2
Matching section M_1		
Maximum β_x-function, m	~ 20	5.4
Maximum β_y-function, m	> 30	6.8
Chromaticity Q'_x	~ 4	0.47
Chromaticity Q'_y	~ 3	0.54
Matching section M_2		
Maximum β_x-function, m	~ 20	6.5
Maximum β_y-function, m	> 30	6.6
Chromaticity Q'_x	~ 4	0.60
Chromaticity Q'_y	~ 3	0.62
Transmission (linear), %	-	25.6
Transmission (nonlinear), %	-	21.8
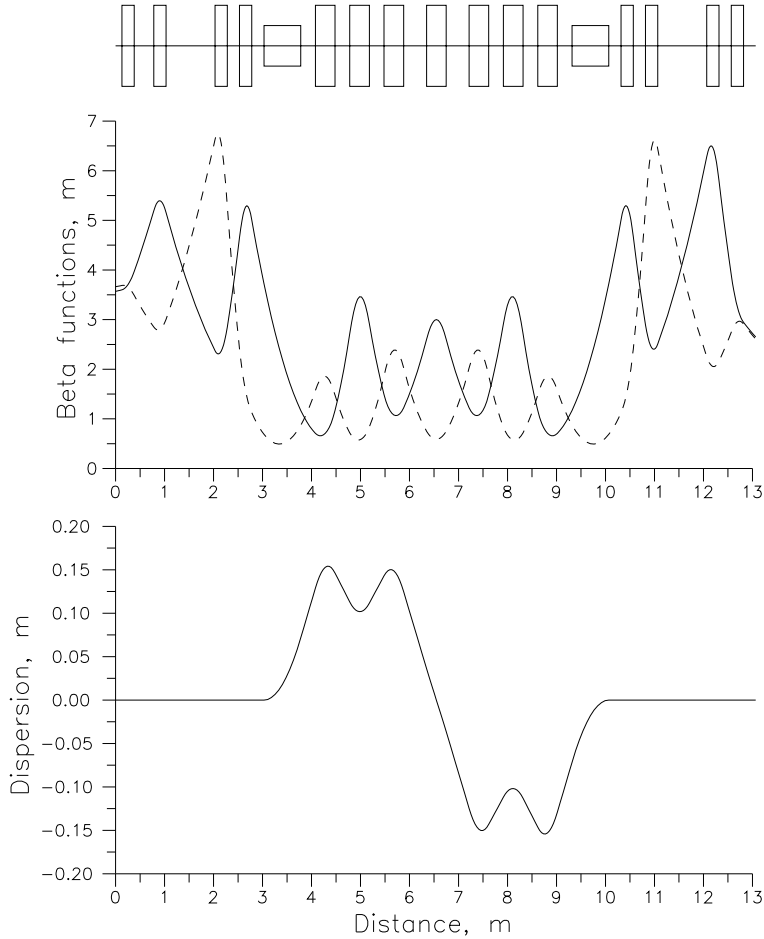
Figure 4.1. Separator structure functions.

plotted before and after the magnetic insertion (separator). It should be noticed here that there is a halo formation in the transverse planes due to nonlinear effects, however the reduction of the positron transmission with respect to the linear matrix tracking is acceptable (Table 4.3).

Taking into account the complex nonlinear particle dynamics in the magnetic insertion, is is apparent that an exact beam collimation is impossible. A rough collimation can be done by using round, straight tubes with appropriate diameters in different parts of the magnetic insertion. The choice of each diameter is determined by the tracks of the particles with an acceptable momentum deviation. Comparing the phase space portraits at (Fig.4.2) and (Fig. 4.3) one can see that aditionally nonlinear effects restrict the beam energy spread after the separator.

In (Fig.4.4) and (Fig. 4.5) the tracking results are presented for particles with momentum deviation less than 15 % and 50 %, respectively, for the positron beam coming into the magnetic insertion after the first accelerating part of the PPA.

The details of the magnetic insertion elements are presented in Chapter 7.1.
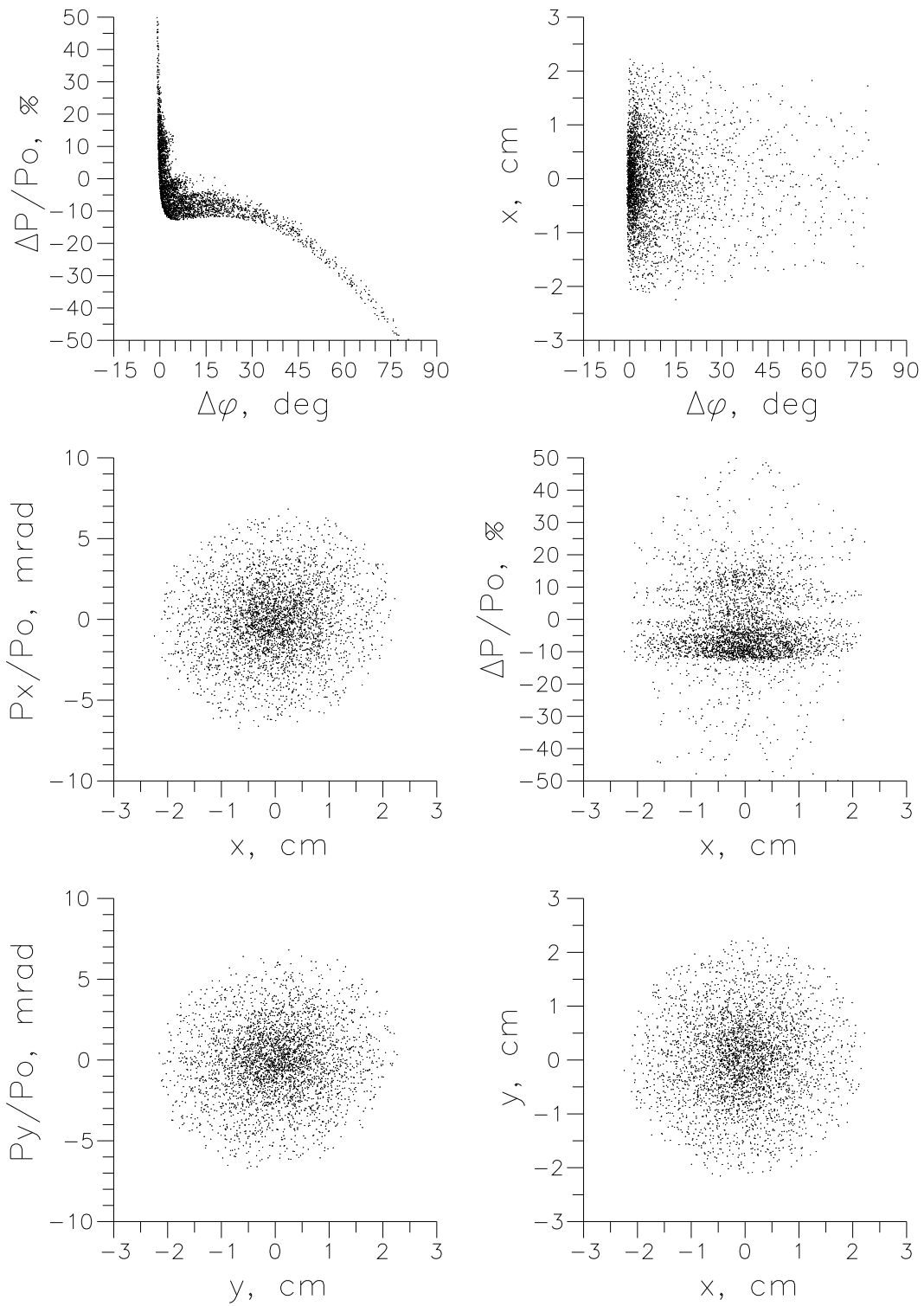
Figure 4.2. Phase space portraits of positrons before the separator.

33
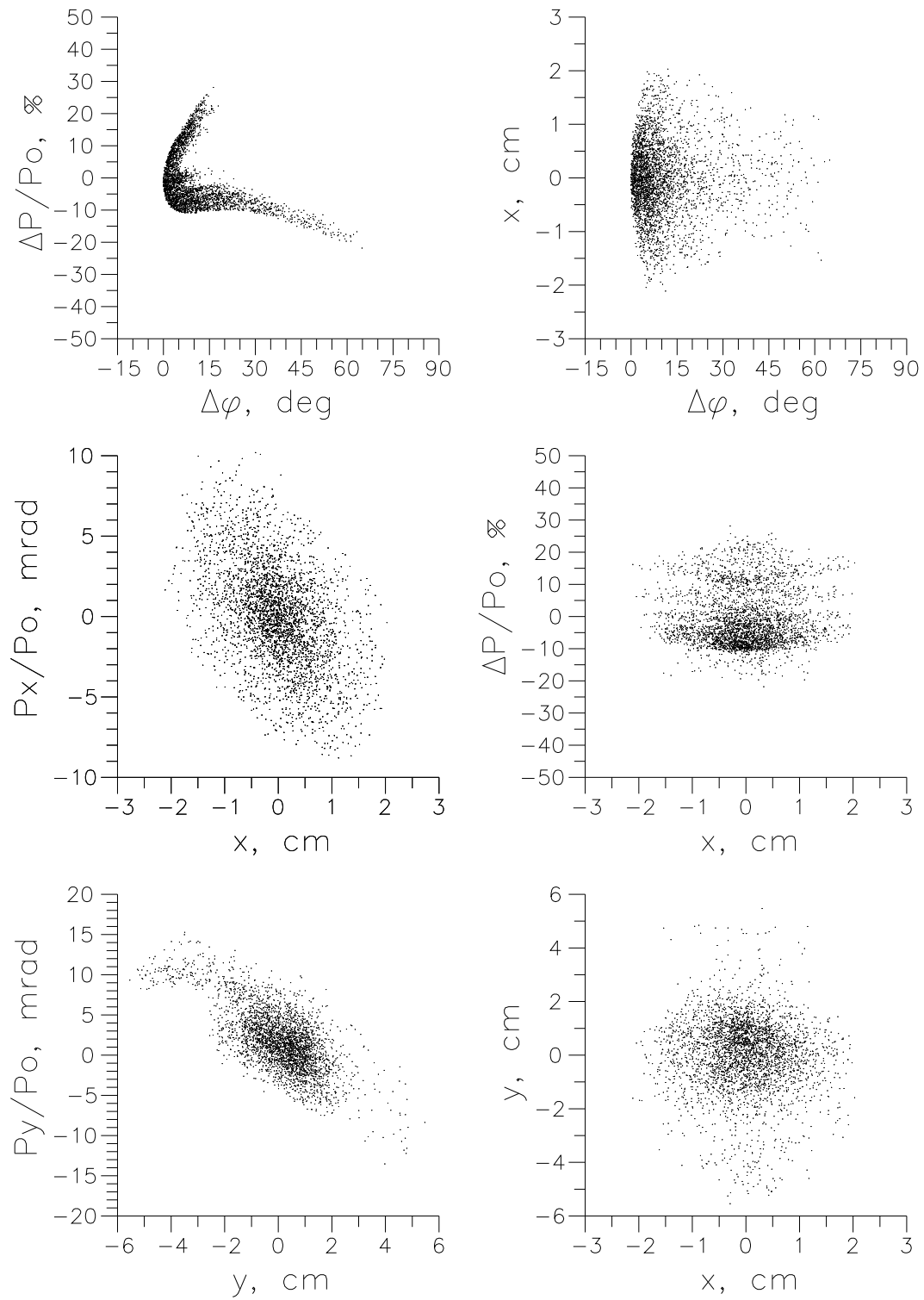
Figure 4.3. Phase space portraits of positrons at the exit of the separator.
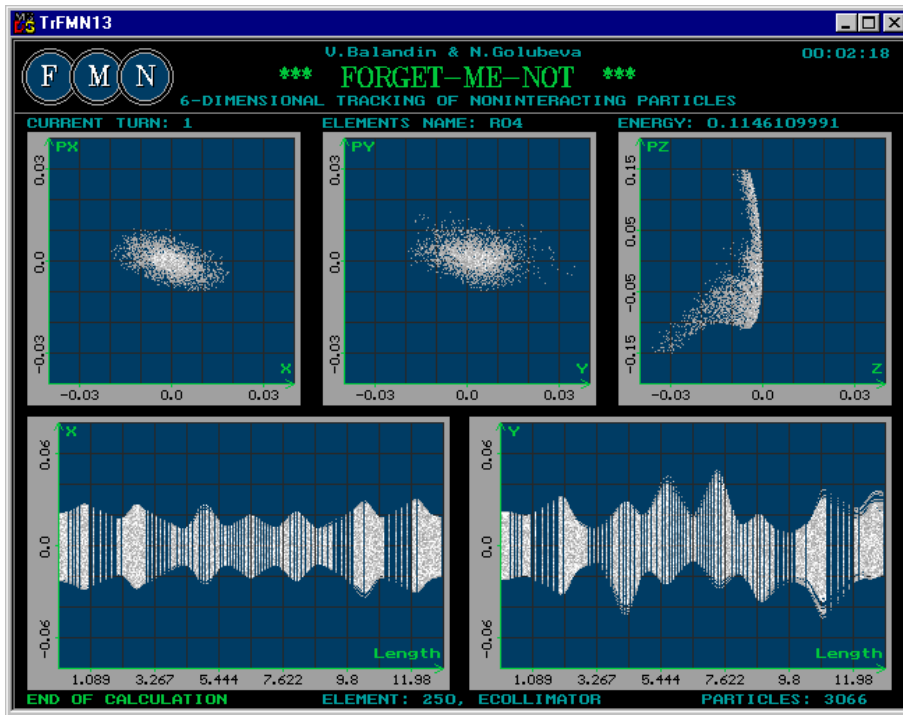
Figure 4.4. Tracking pictures through the insertion for particles with momentum deviation less than 15%.
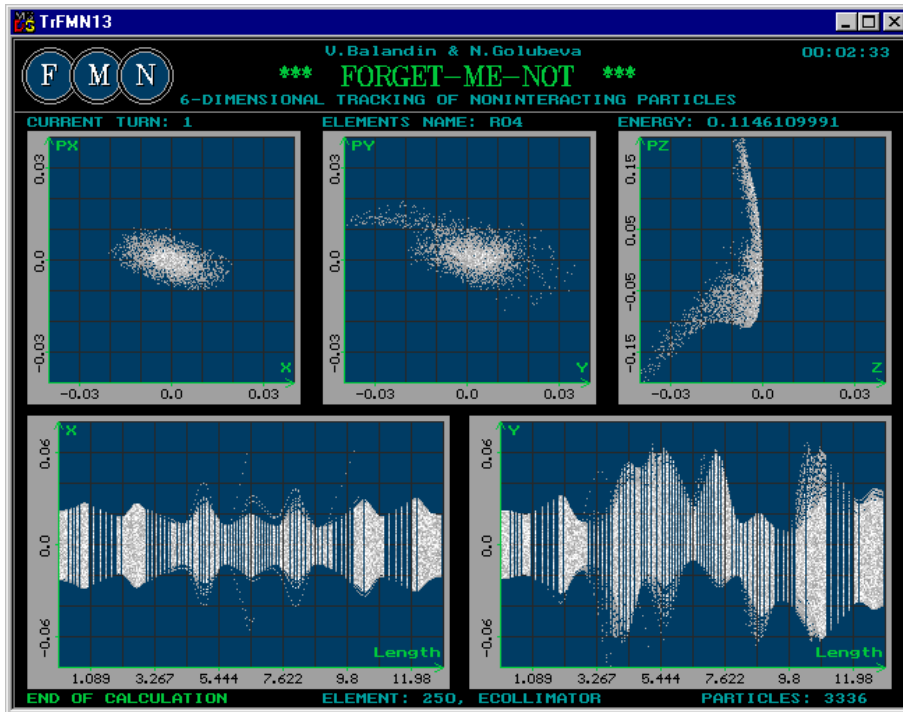
Figure 4.5. Tracking pictures through the insertion for particles with momentum deviation less than 50%.

4.1 Summary

As a result of the study of nonlinear effects on the positron beam dynamics an achromat bending scheme with two bends has been adopted as the basic sheme for the PPA insertion. The presented magnetic insertion scheme has a certain flexibility and permits to realize to bend the beam up by 12.5^o with central trajectory length in the dipoles of more than $0.5m$. This is important for the location and technical design of the separate magnetic elements.

The results of the study also show the importantce of a careful matching between different parts of the PPA magnetic structure.

PPA .... MPA
M1 M2 M0 M5 M6
M0 M3 M4
820 m 48 m 17.3 m
41 FODO cells arc 420 m
21 FODO cells

▮ — bending magnet

M0, M1, M2, M3, M4, M5, M6   —   matching sections

Figure 5.1: Schematic layout of the Long Positron Transport Line.

5   Study of the Long Positron Transport Line

The requirements for the Long Positron Transport Line (LPTL) from the PPA to the MPA are fairly simple. The transport line must:
- use the existing tunnel for the Main Linac, until the design and performance of the transport line is compromised.
- provide a bypass section under the Detector Hall using the beam dump halls. Taking into account that the depth of the experimental hall is 8 m, the translation base between beams must be not less than 15 m.
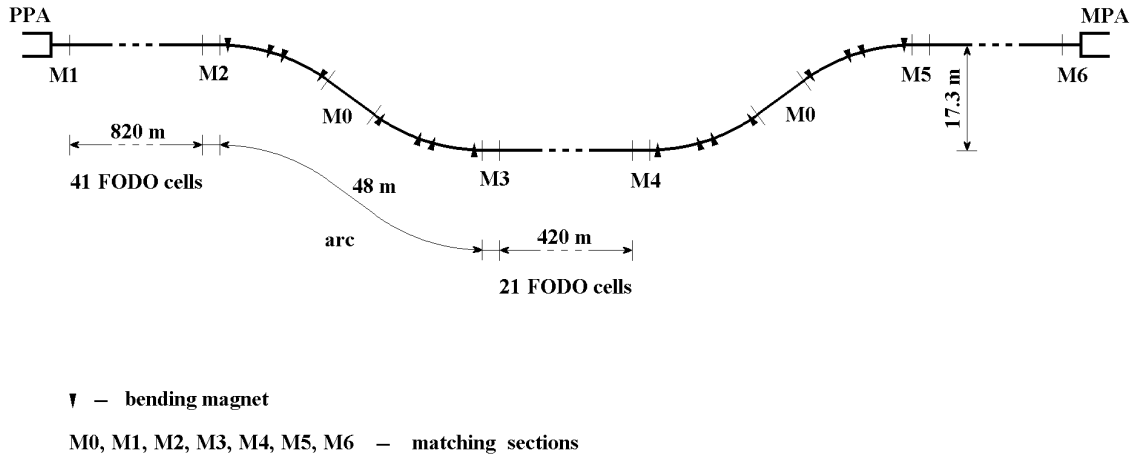- provide adjustable matching with the beam parameters at the PPA exit and MPA entrance.
- avoid to introduce dispersion except for a small part of the bypass section with bends (the bypass section must be achromatic).
- not alter the bunch length (must be isochronous or have a small value of the transfer matrix element R_{56}).
On the other hand there are a few special aspects (see also Table 5.1) which make the task of the beam transport not so simple:
- The transport line is long, so there arises a problem of optimization of the aperture and the number of magnetic elements as well as a problem of design simplicity based on the cost estimation of the beam line.
- The transport line must provide a beam passage with a large transverse emittance and a wide energy spread that:
- gives a large beam size and results in a high aperture of magnetic elements;
- leads to a design of a quasi-isochronous bypass to keep the bunch length constant.
A general LPTL layout is given in (Fig. 5.1). The line has mirror symmetry with respect to the line center (except for the matching sections $M1$ and $M6$ in the beginning and the end). The FODO type magnet structure is used for the long parts of the beam line.

Table 5.1. Main parameters of the transport line

Parameter	Value	Unit
Kinetic energy	287	MeV
Total length	2208.3	m
Length of bypass arc	48	m
Translation base	17.3	m
Normalized emittances		
horiz.	0.036	$m \cdot rad$
vert.	0.036	$m \cdot rad$
Energy spread	± 0.06	

To transport the beam under the experimental hall two similar arcs are used. The first arc transfers the beam down, the second one leads the beam up. The straight beam line between the two arcs is constructed of the same FODO cells as in the main line. The basic LPTL parameters are summarized in Table 5.1.

In this Chapter the linear design for the long transport line is studied. Some aspects of nonlinear dynamics are mentioned in the summary.

5.1   Choise of the periodic structure

For the long straight parts of the transport line a FODO type structure is proposed, based on the simplicity of the design and on the cost-related desire to keep the number of magnets and associated instrumentation small. The parameters of the FODO cell have been chosen basing on some optimum between the maximum of the beam size, the maximum tolerable modulation of the β-function and the number of quadrupoles in the line.

The phase advance of 60° per unit cell is selected to have a small maximum value of the β−function (for a given FODO cell length) and smaller modulation of the β−function. The 90° FODO cell gives us approximately the same maximum value of the β−function and hence the same beam size (the beam radius is 0.047 m), but due to a stronger focusing and modulation of the β−function in the quadrupoles the natural chromaticity of a 90° cell will be larger. From the point of view of the chromaticity minimization the FODO cell with a smaller phase advance will be better (for example, 45° per cell), but then the maximum value of the β-function is increased.

A FODO cell length of $20m$ is selected to keep the maximum of the beam radius not larger than $0.05m$ in the long periodic structure. Shorter cells allow us to reduce the beam size but the number of quadrupoles becomes too large and the chromaticity increases due to a larger number of cells.

Table 5.2 lists parameters of the FODO cell and the number of quadrupoles for all periodic parts of the beam line. The behaviour of the β-functions is shown in Fig. 5.2.

Table 5.2. FODO cell parameters

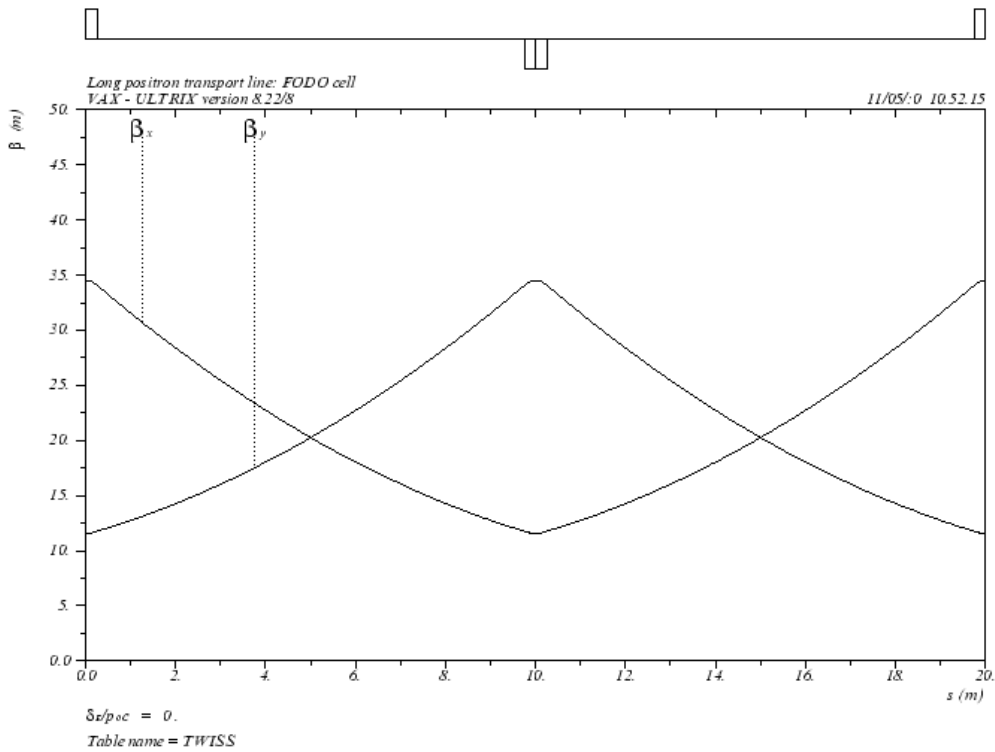| Length of 1 cell (m)	20.0
Phase advance (deg)	$60°$
Length of each quadrupole (m)	0.5
Quadrupole strength $(1/m^2)$	0.2034
Quadrupole gradient (T/m)	0.1954
Maximum beta functions (m)	34.496
Minimum beta functions (m)	11.595
Maximum beam size (radius, m)	0.047
Number of FODO cells	103
Number of quadrupoles	206

Figure 5.2: Behaviour of the optical functions along one FODO cell.

5.2   Bypass section

The desire to use two beam dump halls (the distance between them being $500m$) to bend the beam down and up, prompts the layout of the bypass section: two arcs and a rather long straight section between them which may be constructed of the same FODO cells as the main long transport line (see Fig. (5.1)). Each arc has to lower (or to lift) the beam by a height of not less than $15m$, be achromatic and almost isochronous. Some investigations have been done to find a suitable solution for the arc design which satisfies all the requirements.

The simple design for each arc is an achromatic parallel translation system. The beam is deflected through an angle α by the first bending magnet, the second bending magnet deflects it through an angle $-\alpha$ (the sign of α is reversal for the second arc). The quadrupoles should be put between the two bending magnets to drive the dispersion and focus the beam.

The performed investigations have shown that such an achromatic translation system has some disadvantages for the bypass section - to reduce the dispersion and the path length difference it is desirable to use bending magnets with small angles which together with a large value of the translation base ($h \geq 15m$) give a large number of quadrupoles. For example, for the bending magnets with angles $\alpha = \pm\pi/20$ it is possible to obtain the required translation base using 19 quadrupoles with a maximum dispersion value of about $1m$. If we use the bending magnets with small angles, the lengthening coefficient (the element R_{56} of the linear transfer matrix) will be small.

Following the desire to use a more flexible magnet lattice for the bypass design and taking into account that a FODO type structure is proposed for the long parts of the beam line, some attempts have been made to find such a lattice for the bypass section which is also based on the FODO cells.

As a result of comparison between different lattices, the following design is proposed for the bypass:
- each arc of the bypass section consists of two isochronous cells and a matching section (M0) between them;
- each isochronous cell has an identical FODO type magnet structure, but the dipoles in the second cell have reversed angles to provide the bypass of the interaction point.

5.2.1   Isochronous cell for bypass

The isochronous cell of the bypass is based on a modified four-cell FODO structure with missing magnets [15, 16]. The lattice of the basic isochronous cell and behaviour of optical functions are shown in (Fig. 5.3).

  By taking out some of the bending magnets (the second dipoles in the first and third FODO cells and the first dipoles in the second and fourth ones), we introduce drift spaces, which may generate a negative dispertion region in the two central dipoles. The cell can thus be made isochronous to the first order by tuning the strength of the five quadrupoles (the cell has mirror symmetry with respect to the center of the fifth quadrupole) in such a way that the integral of D_y/ρ over the two central dipoles exactly cancels the same integral over the two lateral ones.

The dispersion D_y is positive and may be rather high in the missing magnets region but its contribution to the matrix element R_{56} is zero since ρ is infinite there. In our case it is
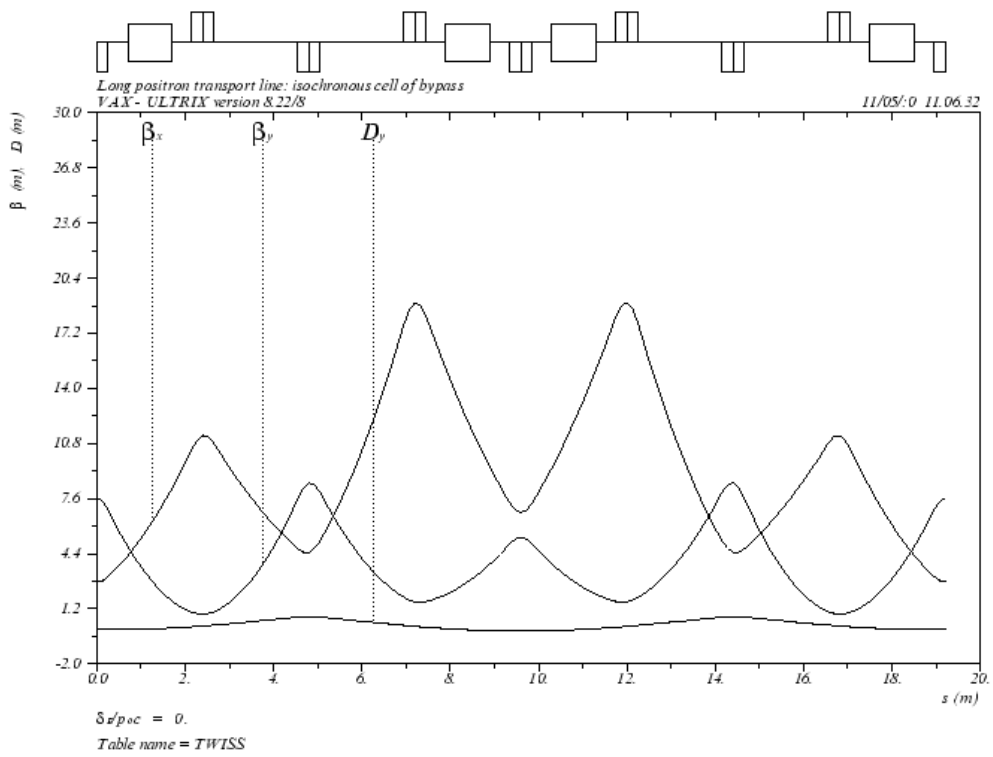
Figure 5.3: Lattice of the basic isochronous cell.

Table 5.3. Structure of one half of the quasi-isochronous cell

		Length, m	Bending angle	Strength k_1, $1/m^2$
Quadrupole	q1	0.50		-1.4929970
Drift		0.45		
Dipole	bd1	1.00	9°	
Drift		0.45		
Quadrupole	q2	0.50		+0.8935050
Drift		0.45		
Drift	lbd	1.00		
Drift		0.45		
Quadrupole	q3	0.50		-1.3556050
Drift		0.45		
Drift	lbd	1.00		
Drift		0.45		
Quadrupole	q4	0.50		+0.8769116
Drift		0.45		
Dipole	bd1	1.00	9°	
Drift		0.45		
Quadrupole	q5	0.25		-1.1762750

desirable to make the dispersion as small as it is possible to reduce the beam size which may be large due to a large value of energy spread of the positron beam ($\pm 6\%$).

If other elements in the transport line (in our case, the lengthening of a long FODO structure, which is $L/(\beta_0\gamma_0)^2 \simeq +0.007m$ for $L = 2200m$ and the kinetic energy 287 MeV) have a small non-zero R_{56}, the transport line can be tuned to be quasi-isochronous, its residual R_{56} being of such a value that the sum of the individual contributions is zero. Taking into account that it will be good to have a small negative value of R_{56} for all the previous parts before the MPA, the value $R_{56} = -0.01m$ is chosen for the long transport line, that gives $R_{56} = -0.0042m$ for each cell in the bypass. There is no problem to obtain any desirable value of the linear transfer matrix element R_{56} for the LPTL only by tuning the strengths of the quadrupoles in the quasi-isochronous cells in the bypass. Table 5.3 shows the structure of one half of the quasi-isochronous cell. Table 5.4 lists parameters of the quasi-isochronous cell and the matching section M0 of the bypass.

5.2.2 Arcs of bypass

Each arc of the bypass section consists of two isochronous cells. Each of them deflects the beam through the same angle but in reverse directions and the matching section $M0$ between them. Each cell in the arc deflects the beam by an angle of 36°, that gives the translation of the beam to a depth of $5.4m$. To obtain the required translation base not smaller than $15m$, a matching section between two cells is needed. It is convenient to make this matching section consisting of the same FODO cells (without bending magnets) as an isochronous cell. Two FODO cells 4.8 m long each, allow one to obtain the translation base equal to 17.3 m.

Table 5.4. Bypass parameters

	bypass cell	matching section
Length of 1 cell (m)	19.2	4.8
Number of dipoles	4	
Length of each dipole (m)	1.0	
Bending angle of each dipole	9°	
Dipole Field (T)	0.151	
Number of quadrupoles	8	4
Length of each quadrupole (m)	0.5	0.5
Maximum quadrupole gradient (T/m)	1.432	1.405
Momentum compaction R_{56} (m)	-0.0042	
Maximum beta functions (m) horiz. vert.	18.965 8.488	11.161 8.497
Maximum dispersion (m)	0.739	
Maximum beam size (radius, m)	0.068	0.027

The behaviour optical functions along one bypass arc is shown in (Fig. 5.4).

5.3 Matching sections

Between the exit of the PPA linac, the entrance of the MPA and the FODO structure the matching sections $M1$ and $M6$ are used. There are also matching sections between the FODO structure and the bypass arcs. All matching sections consist of four quadrupoles. Due to the length fitting the lengths of the matching sections $M2$ and $M3$ at the entrance and at the exit of each arc are different in lengths.
Parameters of all the matching sections are listed in the Table 5.5.

5.4 Beam size and aperture of quadrupole magnets

The maximum beam size in quadrupole lenses is calculated as the maximum upper limit:

$$(x, y)_{max} = \sqrt{(\beta_{x,y})_{max} \cdot \varepsilon_{x,y}} + D_x \frac{\Delta W}{W_c} \tag{24}$$

where $\varepsilon_{x,y}$ are the total emittance values in the transverse planes and $\frac{\Delta W}{W_c}$ is the particle energy spread (see Table 5.1).
The beam size values in the FODO structure and in the bypass section are listed in Table 5.6. In the matching sections the maximum $\beta-$function is not allowed to be larger than in the FODO cell.

The diameter of the aperture for quadrupole lenses may be chosen equal to 0.16 m, that gives us an aperture safety factor equal to 1.7 for the FODO cells and more than 2 for all bypass quadrupoles, except for two quadrupole in each bypass cell ($q3$), in which the dispersion reaches its maximum value (0.74 m). The aperture safety factor for these 8 quadrupoles ($q3$) is approximately 1.2. If this value is not sufficient, it is possible to
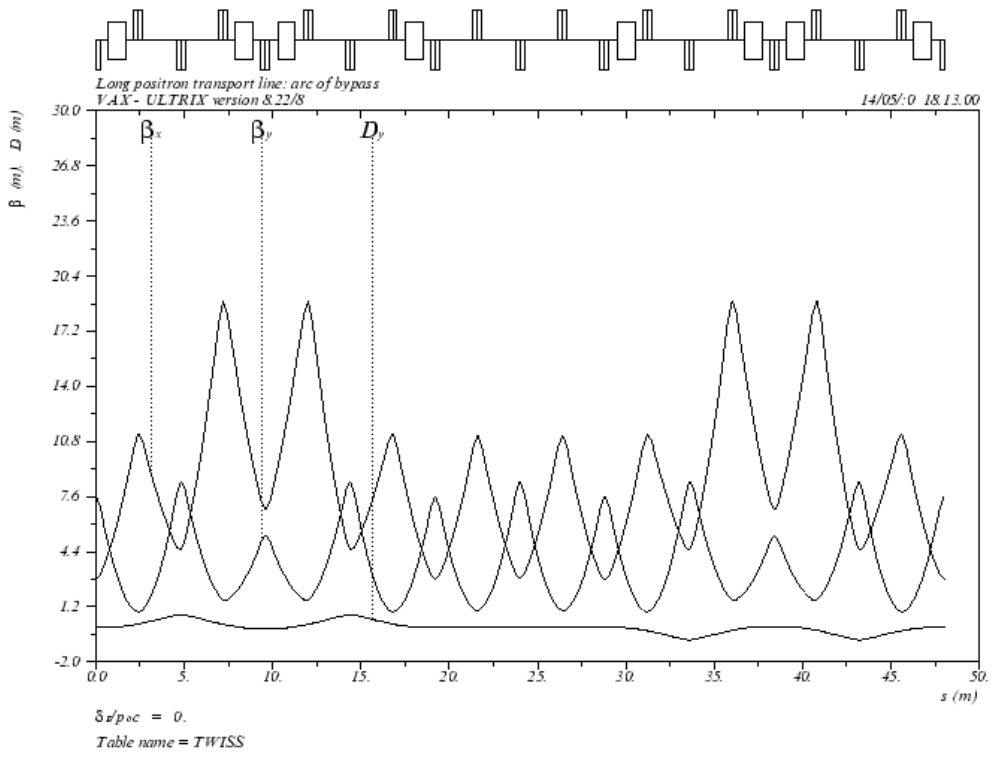
43

Figure 5.4: Behaviour of optical functions along one bypass arc.

Table 5.5. The structure of matching sections

		Length, m	Strength, k_1 $1/m^2$
Matching section 1		7.0	
Drift		1.0	
Quadrupole	q1m1	0.50	+0.6111415
Drift		0.6	
Quadrupole	q2m1	0.50	-0.3754501
Drift		1.8	
Quadrupole	q3m1	0.50	-0.7896255
Drift		0.6	
Quadrupole	q4m1	0.50	+0.6072866
Drift		1.0	
Matching section 2		7.05	
Quadrupole	q1m2	0.50	+0.8125865
Drift		0.6	
Quadrupole	q2m2	0.50	-1.1596300
Drift		2.35	
Quadrupole	q3m2	0.50	+0.6900151
Drift		0.6	
Quadrupole	q4m2	0.50	-0.2254244
Drift		1.5	
Matching section 3		11.85	
Drift		2.85	
Quadrupole	q1m3	0.50	+0.7402444
Drift		2.0	
Quadrupole	q2m3	0.50	-0.6277262
Drift		3.0	
Quadrupole	q3m3	0.50	-0.2445018
Drift		2.0	
Quadrupole	q4m3	0.50	+0.3989359
Matching section 6		7.0	
Drift		1.0	
Quadrupole	q1m6	0.50	+0.6769593
Drift		0.6	
Quadrupole	q2m6	0.50	-1.0072680
Drift		1.8	
Quadrupole	q3m6	0.50	+0.4512171
Drift		0.6	
Quadrupole	q4m6	0.50	-0.2871149
Drift		1.0	

Table 5.6. Parameters of quadrupole lenses (FODO cells and bypass section)

|	Length, m	Strength, $1/m^2$	Maximum beam size, m	Diameter of aperture, m	Number
FODO cell	0.5	$\pm$ 0.2034218	0.047	0.16	206
Bypass arc					
q1	0.5	-1.4929970		0.16	8
horiz.			0.013		
vert.			0.022		
q2	0.5	+0.8935050		0.16	8
horiz.			0.027		
vert.			0.019		
q3	0.5	-1.3556050	0.068	0.16	8
horiz.			0.017		
vert.			0.068		
q4	0.5	+0.8769116		0.16	8
horiz.			0.035		
vert.			0.021		
q5	0.5	-1.1762750		0.16	8
horiz.			0.021		
vert.			0.022		
q2m	0.5	+1.013745		0.16	4
horiz.			0.027		
vert.			0.008		
q3m	0.5	-1.464863		0.16	4
horiz.			0.013		
vert.			0.023		
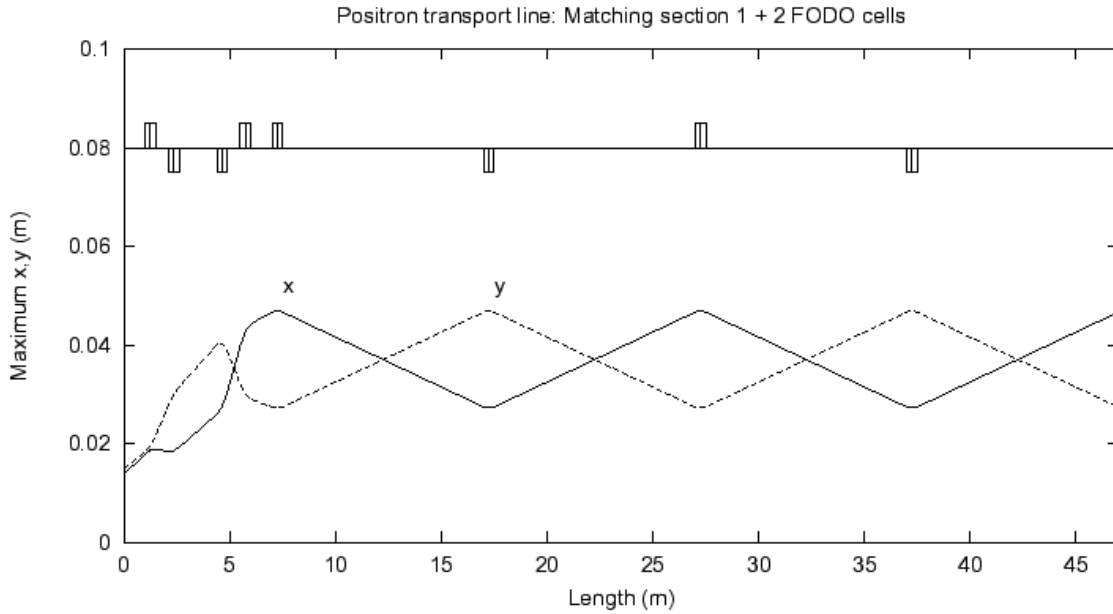
Figure 5.5: Beam envelopes along the matching section 1 and two adjacent FODO cells.

increase the aperture for $q3$ quadrupoles up to 0.20 m to obtain a safety factor equal to 1.5. But this place might also be used for longitudinal momentum collimation.

The beam envelopes for some particular LPTL parts (the matching sections and the arcs), obtained with estimations (24), are shown in (Fig. 5.5.- 5.9).

5.5 Beam collimation

Efficient protection of the MPA linac against losses of both on-momentum and off-momentum particles requires two collimation system: one with a zero dispersion function (to limit the transverse particle amplitudes) and a second with a large dispersion (to limit the momentum spread values).

The betatron collimators are used to limit the transverse particle amplitudes. They must be located at large values of the $\beta-$functions to maximize the impact parameters. Equally, the transverse amplitude limit set by collimators should be the same for all momentum values. This implies zero dispersion values at the collimators. Without any problems the betatron collimators can be located in the long straight parts of the LPTL.

The momentum collimation of particles with large momentum spread can be done in the arcs of the bypass section with the dispersion. The momentum collimators can be located in the high-dispersion regions corresponding to the missing magnets (see Fig. 5.4, Fig. 5.7). Comparing plots in Fig. 5.4 and Fig. 5.7 one sees, that the main part of the beam envelope growth in the y-plane is due to dispersion.

The optimum placing and parameters of the collimators have to be determined by tracking, in general, taking into account the nonlinear effects and in the presence of all multipole and alignment errors.
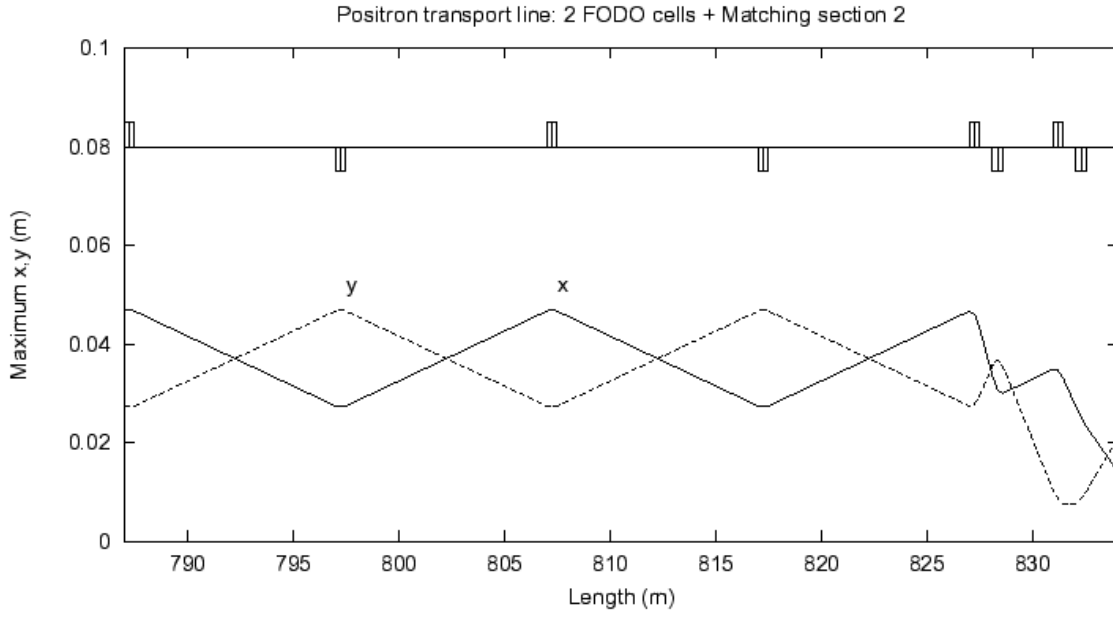
47

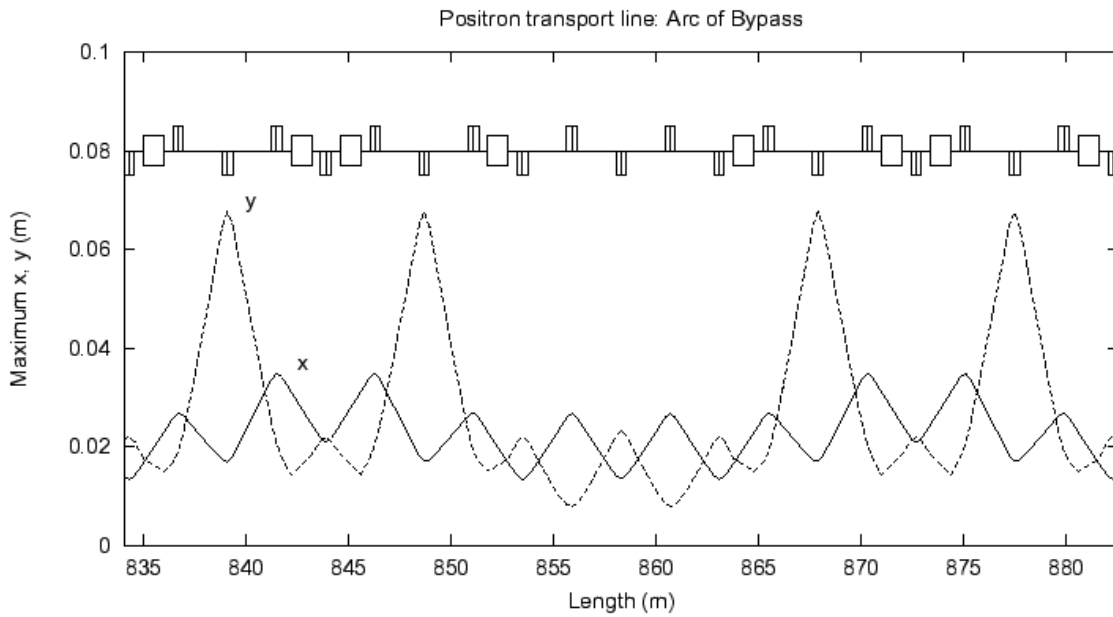Figure 5.6: Beam envelopes along the matching section 2 and two adjacent FODO cells.

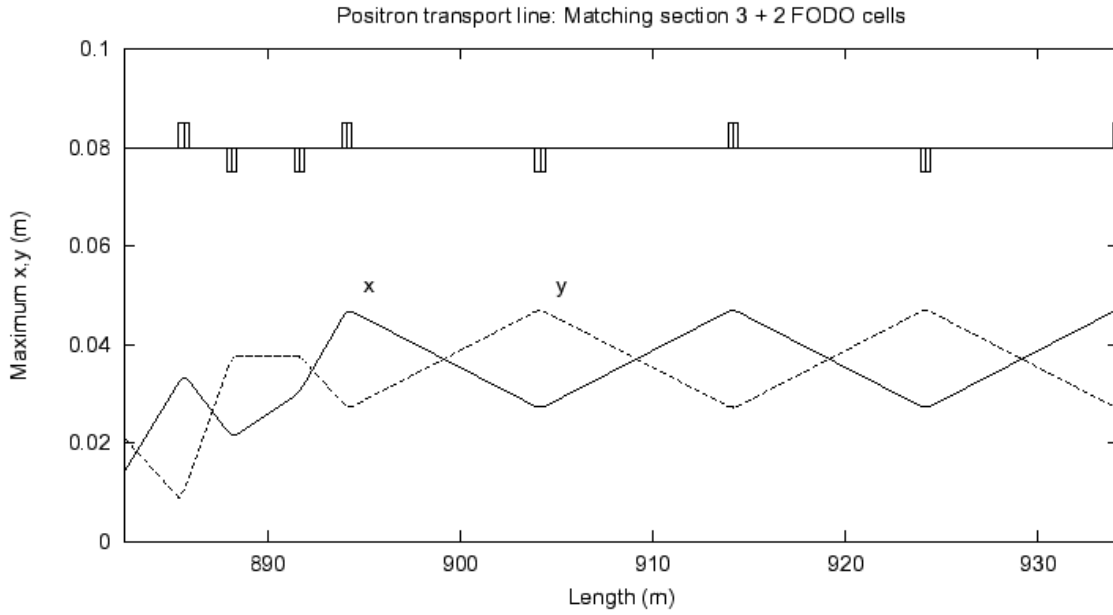Figure 5.7: Beam envelopes along one of the bypass arcs ($\Delta E / E_0 = \pm 6\%$).

Figure 5.8: Beam envelopes along the matching section 3 and two adjacent FODO cells.
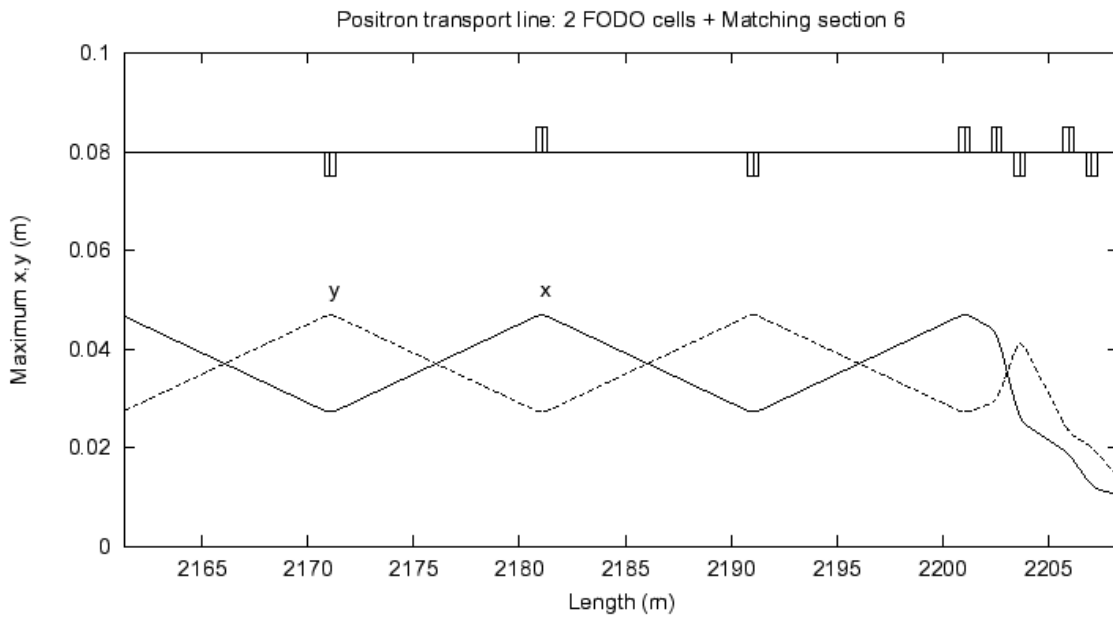

Figure 5.9: Beam envelopes along two last FODO cells and the matching section 6.

49

5.6 Summary

For the Long Positron Transport Line a FODO type structure is proposed for the long straight parts as well as for the bypass section. Due to the dispersion in the bypass cells the length of the FODO cell in the bypass is chosen approximately 4 times shorter than for the periodic lattice to keep the beam size be low than $0.05m$ (except of 8 quadrupoles). The LPTL consist of several parts, and the same type of the magnet lattice allows one to simplify matching between different LPTL parts.

The diameter of the aperture for the all quadrupole lenses is equal to 0.16 m, providing a aperture safety factor of 1.7 for the FODO cells and more than 2 for all the others quadrupoles. This choise is a reasonable compromise between a reasonable safety factor and the number of magnetic elements.

A flexible solution is proposed for the bypass sections, allowing to tune momentum compaction factor and to tune the LPTL as an isochronous or a quasi-isochronous (in the first order) line in total.

It should be noted that it is possible to use triplet cells for the long periodic parts of the transport line. In this case the number of magnets per unit cell increases (three magnets instead of two in a FODO cell), but there are some advantages of the triplet lattice: smaller β-functions modulation in quadrupoles magnets leads to smaller chromaticity, reducing the distortions in the longitudinal phase space. But in the case of using the FODO type structure for the isochronous bypass matching between two different types of magnet lattice is more difficult and can cancel the advantage of the smaller triplet structure chromaticity.

A study of nonlinear effects in the LPTL was not foreseen at the present stage. Nevertheless, an estimation has been performed in the same way as for the PPA magnetic insertion (see Chapter 4). The results show a visible reduction in the positron transmission, but it is not so drastical to cancel the present LPTL design completely. If at the PPA exit the useful positrons number is $\approx 21.3\%$, after the PPA and LPTL it is reduced to $\approx 16\%$. It is reasonable close to the estimated requirement [3] ($\approx 17\%$) for the total positron injector, especially taking into account a safety margin for the PPA of 2.5 instead of the usual value 2.

It should be pointed out here again, that for the LPTL we have a unique combination of requirements:
- the positron beam has both a large transverse emittance and a wide energy spread,
- the LPTL is a long line with bypass sections, must have parts with different magnetic structures, matching sections and contains a significant number of magnetic elements.

Under these conditions the nonlinear effects should provide a strong influence and it allows us to point out the reduction from $\approx 21.3\%$ to $\approx 16\%$ as tolerable and consider the present design as the basic LPTL proposal.

But this reduction is quite sufficient to stimulate a futher LPTL study to diminish its value. A set of topics, related with nonlinear beam optics, such as:
- the investigations of chromaticy effects in the long straight parts and bypass section;
- the study of transverse nonlinearities;
- the effects of the matching sections;
- the higher order isochronicity,

together with all multipole and alignment errors should be the next step of the LPTL development.

Table 6.1: TESLA and TTF element characteristic parameters.

Element	Parameter	Value
Accelerating section	Length, mm	1276
	Number of cells	9
	Energy gain, MeV/m	25
	Iris diameter, mm	70
Quadrupole	Maximum gradient, T/m	60
	Effective length, mm	520
	Total assembly length, mm	874
	Inner diameter, mm	78
TTF doublet	Maximum gradient, T/m	20
	Effective quadrupole length, mm	150
	Total assembly length, mm	630
	Inner diameter, mm	78

6 Study of the Main Positron linac design.

To be injected into the Damping Ring the positron beam must be accelerated up to ($\approx 5\,\mathrm{GeV}$ [1]. The beam energy at the PPA output is planned to be $250 \div 300\,\mathrm{MeV}$. Behind the PPA is a Long Positron Transport Line followed by a superconducting high accelerating gradient linac - the Main Positron Accelerator (MPA), based on the standard TESLA superconducting structure [1].

The main purpose of the present study is to design the MPA proposal using as many elements elaborated for the TESLA [1] and TTF [22] projects as possible.

It should be pointed that the application of the TESLA FODO solution for the transverse focusing structure is impossible because of the large transverse emittances for the positron beam (see Chapter 2). The acceptance requirements on the positron beam transverse emittances (3) is approximately by three orders of magnitude greater than those on the electron beam emittances for TESLA [1] and TTF [22]. Moreover, the requirements of the MPA safety demands that the beam dimensions be as small as possible.

Taking into account the TTF experience [22], the study has been done mainly for the doublet quadrupole assembly to fulfil the transverse focusing structure.

There are only two types of cryomodule designs in consideration for the TESLA project [23] instead of the seven types for the earlier proposal [1]. The first type consists of eight standard TESLA accelerating sections (AS) and the second one has an additional superconducting quadrupole. Some specific parameters of the AS [1] and the quadrupole [23] are collected in Table 6.1. as well as the TTF doublet parameters [22]. The considertion shows the possibility to realize a quadrupole doublet on the base and with the same length as the new TESLA quadrupole [23]. Its schematic picture and a superconducting AS view are presented in Fig.6.1. It is possible to keep the doublet field parameters, mentioned in Table 6.1 [23], except for the effective field length, which is estimated as $\sim 200\,\mathrm{mm}$ for each quadrupole [23]. To consider different focusing schemes, it was suggested that some ASs in the standard TESLA cryomodule design may be replaced by the proposed
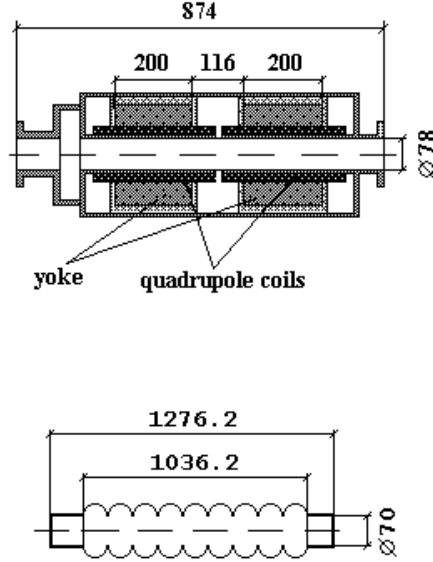
Figure 6.1.: Schematic view of the quadrupole doublet and rf-section.

quadrupole doublet. In this case the doublet length should be increased up to the AS length by adding drifts for the quadrupole assembly.

In (Fig.6.2) two different options for a cryomodule configuration are presented. The first one should be used at the MPA beginning. Here four Quadrupole Doublets (QD) and four AS are placed inside the cryomodule, its type is referred to as Cryomodule♯1. In the standard TESLA design this cryomodule type contains eight ASs [23]. The second configuration is the standard TESLA cryomodule (Cryomodule♯2)[23] with a quadrupole replaced by the proposed quadrupole doublet.

To fulfil the transverse periodic focusing different combinations of the AS and QD can be used. Taking into account the cryomodule type designs only three combinations were chosen as basis. They can be described briefly as follows:

Cell♯1: AS-QD. Four of these cells can be placed in Cryomodule♯1.

Cell♯2: 3*AS-QD. Two of these cells can be placed in Cryomodule♯1.

Cell♯3: 8*AS-QD. This cell can be placed in Cryomodule♯2.

In (Fig.6.3) the maximum value of the envelope β-function and phase advance μ per unit cell for the periodic solution are presented depending on the quadrupole strength. At Fig. 6.3 the solid lines are for the periodic line consisting of the Cells♯1, long dashed lines are for Cells♯2 and short dashed lines - for Cells♯3. It should be noted that all these curves are adequate both for horizontal and vertical planes.

Keeping in mind the requirement that the beam dimension should be smallest, the cell parameters of Table 6.2 were chosen for consideration. For these parameters the
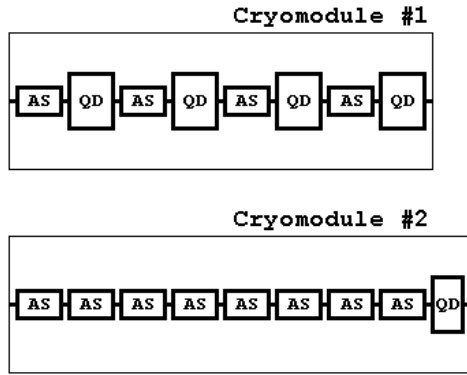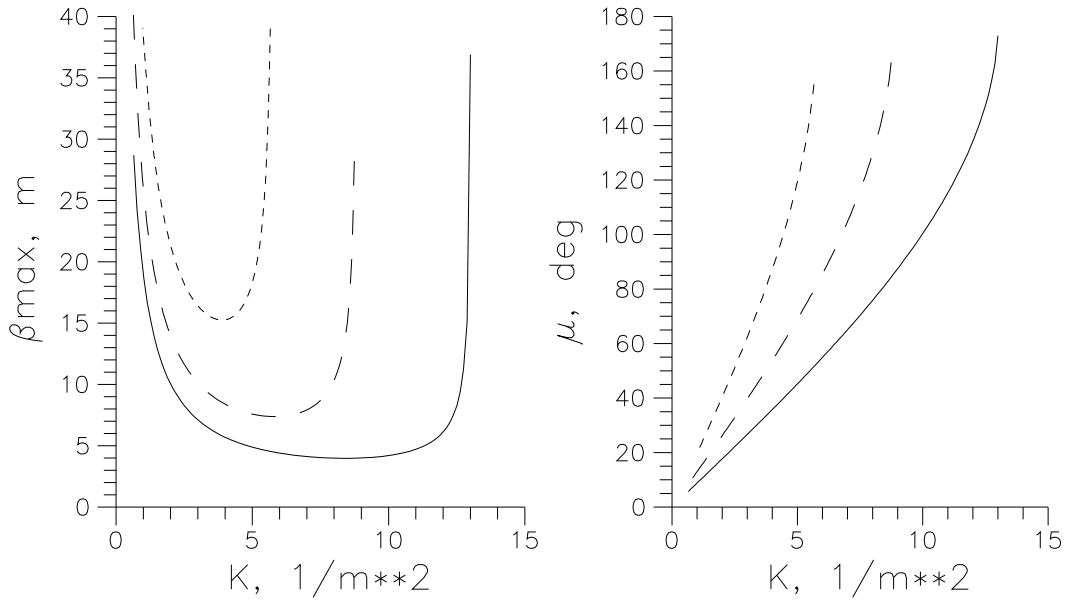
Figure 6.2. Cryomodule types.

Figure 6.3. Structure functions for the different periodic configurations.

Table 6.2: Possible MPA cells characteristic parameters.

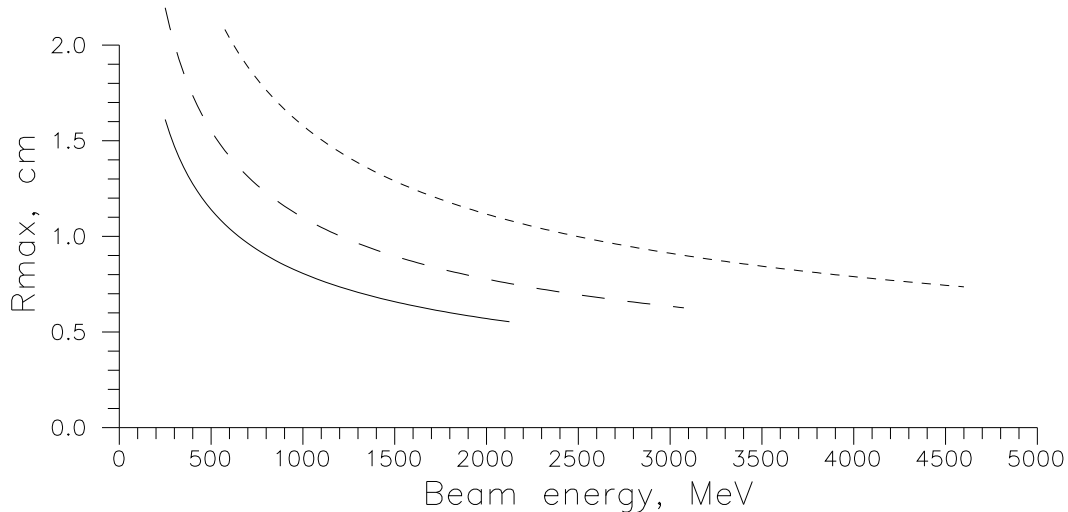| Parameter	Cell ♯1	Cell ♯2	Cell ♯3
Quadrupole strenght k, m^{-2}	8.43	5.92	4.00
Phase advance μ, deg	80.7	84.2	87.5

Figure 6.4. Beam size with respect to the beam energy for the different periodic configurations.

behaviour of the maximum beam envelope is plotted in Fig.6.4 according to the beam energy for the different periodic structures. The calculations were made for beam emittances $\varepsilon_x = \varepsilon_y = 0.036$ m. The high energy ends of the curves are referred to the maximum quadrupole gradient mentioned in Table 4.1. This picture and the following assumptions are the base to make a preliminary design of the MPA. If the beam energy at the PPA exit is expected to be ~ 280 MeV the MPA beginning must be constructed from Cell$\sharp$1 to minimize the beam dimensions. It is known that one standard TESLA rf-klystron can feed 32 ASs with a beam energy gain of ~ 25 MeV per AS [1]. Therefore if the MPA beginning will consist of 32 Cells$\sharp$1 for a uniform rf-power klystron loading the final beam energy after this part will be ~ 1080 MeV. Apparently it is not reasonable to use Cells$\sharp$2 for further acceleration, firstly due to rf-feeding problems (new rf-feeding scheme for cryomodules) and secondly because the transition to the Cell$\sharp$3 structure is later absolutely necessary. Moreover the beam dimensions for the Cell$\sharp$3 structure are acceptable at the energy pointed above. Finally, the MPA basic design looks like the first part based on Cell$\sharp$1 (32 cells or 8 Cryomodules$\sharp$1) and the second part constructed from Cell$\sharp$3 (Cryomodules$\sharp$2) up to the desired energy (~ 5 GeV).

In Fig.6.5 the structure β-functions are plotted for the first eight cryomodules. A violation of the cell periodicity at the ends of the cryomodules was taken into account. The eighth cryomodule is used for matching. In Fig.6.6 structure β-functions are plotted for the cryomodules of the second MPA part.

In addition it should be noted that the possibility to use the standard TTF doublets [22] was studied. Their parameters are listed in Table 4.1. In this case at least two matching transitions and three different periodic cell constructions will be needed. Moreover there will be problems with the rf-feeding and symmetry of the power loading for two klystron outputs. This MPA design can not be recommended.

Another possibilities for the MPA design should be pointed out:
- It is possible to use longer quadrupoles (~ 400 mm) for the doublets in order to exclude the additional drifts when the ASs are replaced by doublets. In this case only Cryomodules$\sharp$1 are used and there is a reserve in the qudrupole strength, for higher beam
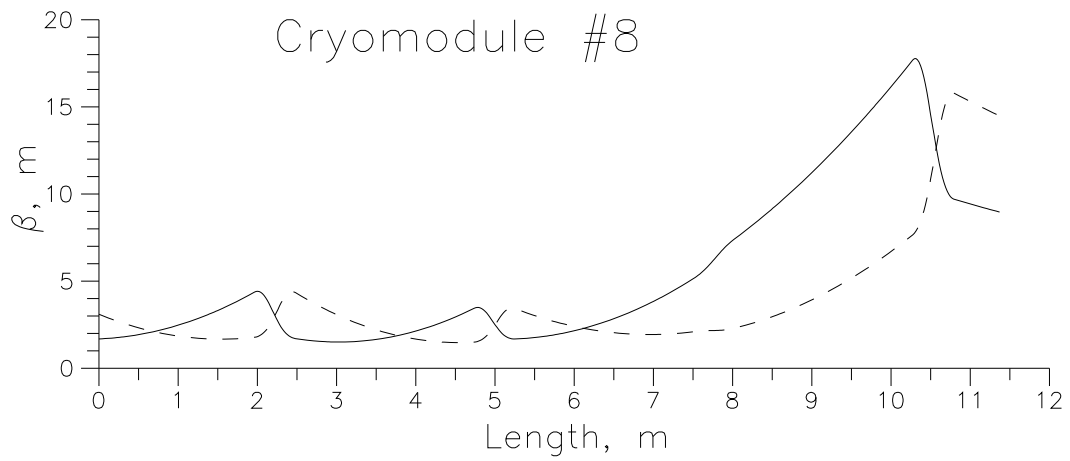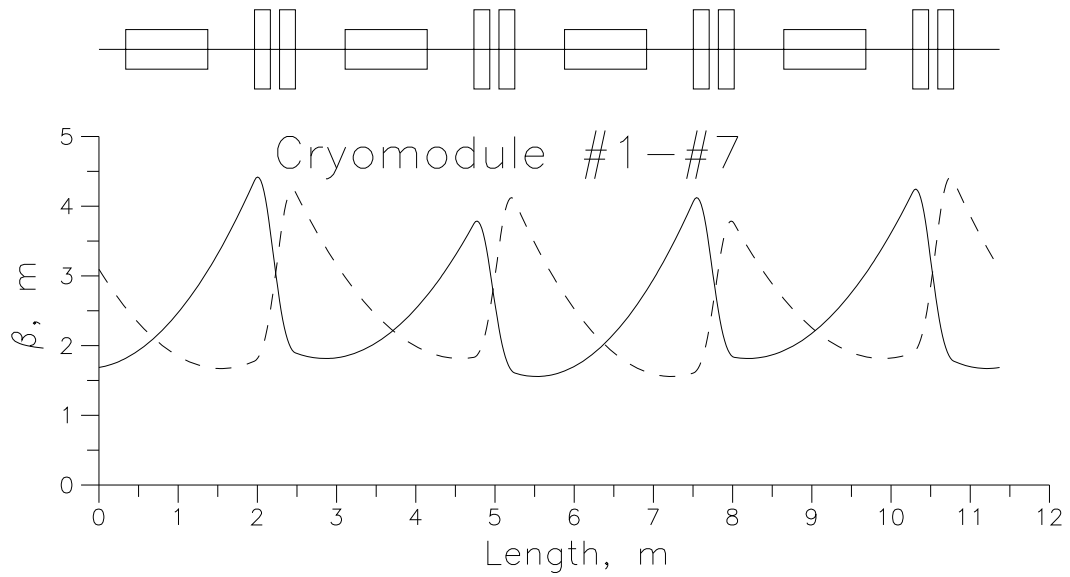
54

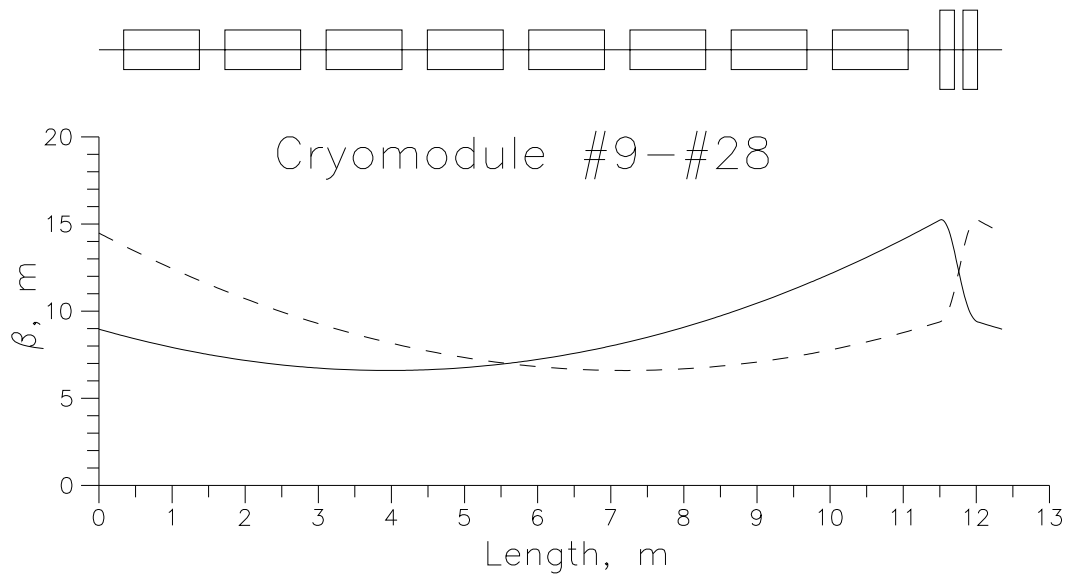Figure 6.5. Structure β-functions for the first eight cryomodules.

Figure 6.6. Structure β-functions for the main part of cryomodules.

energies mainly. Hovewer the average beam energy gain is slightly reduced with respect to the basic MPA design, because Cryomodules ♯2 are not used and the QD replaces the last AS in each Cryomodule ♯1 of the second MPA part. As a results of this demerit there will be a reduced power operation for the klystrons of the second part or an increased energy gain for the second part ASs if the klystrons will the nominally powered.

- It is possible to use quadrupole triplets with longitudinal dimension as for ASs and field parameters as for the quadrupole from Table 4.1. Fig.6.5 shows it is possible to use the Cell ♯2 structure with triplet transverse at the first MPA part without any growth in beam dimensions. Apparently, this variant has certain advantages over the basic MPA design. However a technical study of the triplet construction is necessary.

6.1   Summary

Different transverse focusing structures have been considered for the MPA design. Results of the study show the possibility of an MPA design with doublet quadrupole assembly to fulfil the transverse focusing structure and keep the beam size limited with a safety margin of 2. The doublet assembly can be made basing on the the new TESLA superconducting quadrupole.

Two types of the standard TESLA cryomodules are used in MPA. In the first MPA part, with positron energy up to $\approx 1 GeV$, the standard TESLA 9 cell accelerating sections can be applied only. For the second MPA part the "super-structure" - 4 sections with 7 cells each can be considerd.

Table 7.1.1: AMD basic parameters

Length, m	~ 0.89
Initial magnetic field, T	6
Final magnetic field, T	0.22
Taper parameter, m^{-1}	29.5
AMD-solenoid entering, m	~ 0.6

7 Proposal for the TESLA Positron Injector Parameters

Basing on results of the investigations, described in Chapter 2 - Chapter 6, the proposal for the different positron injector parts, technical details and general parameters are summarized below.

7.1 Updated PPA parameters

The general PPA concept and scheme doesn't change in comparison with the previous proposal [2].

The principal PPA scheme consists of the following parts:

- the adiabatic matching device (AMD);
- the first acceleration part embedded in a uniform solenoid field and put into the AMD at the beginning;
- the magnetic insertion system (separator) to shift the positron beam axis to a parallel line displaced from its original location by a distance of $1.0 \div 1.2$ m, to separate the electrons and photons and, in addition, to clean the positron beam from the unacceptable particles;
- the second acceleration part with transverse triplet focusing.

A general PPA layout is shown in Fig. 7.1. Further a brief description of the elements and characteristics for each PPA part is presented.

AMD. Its detailed description is presented in [3] except for the fact that the ending part of the AMD may be combined with the following solenoid. The proposed AMD parameters are listed in Table 7.1.1.

The first PPA part. It consists of four Acceleration Cavities (AC) embedded in a focusing solenoid. The first two ACs have a high accelerating gradient whereas the others have a moderate one. Each cavity is powered by one klystron. The cavities are separated by a drift space of λ_{rf}. Parameters of the high gradient (Type ♯1) and moderate gradient (Type ♯2) cavities are listed in Table 7.1.2.

The basic design and operation parameters for the first PPA part are collected in Table 7.1.3.

Insertion - separator. Its structure is "matching part - bending part - matching part". In detail this magnetic system is discussed in Chapter 3. The proposed characteristics of the elements for different system parts are presented in Table 7.1.4. The total positron losses in the separator can be estimated as $\sim 8.4\,\%$ of the incoming positron beam. These losses are composed mainly from the particles with a large momentum deviation with respect to the magnetic system central energy. Behind the first dipole of the separator
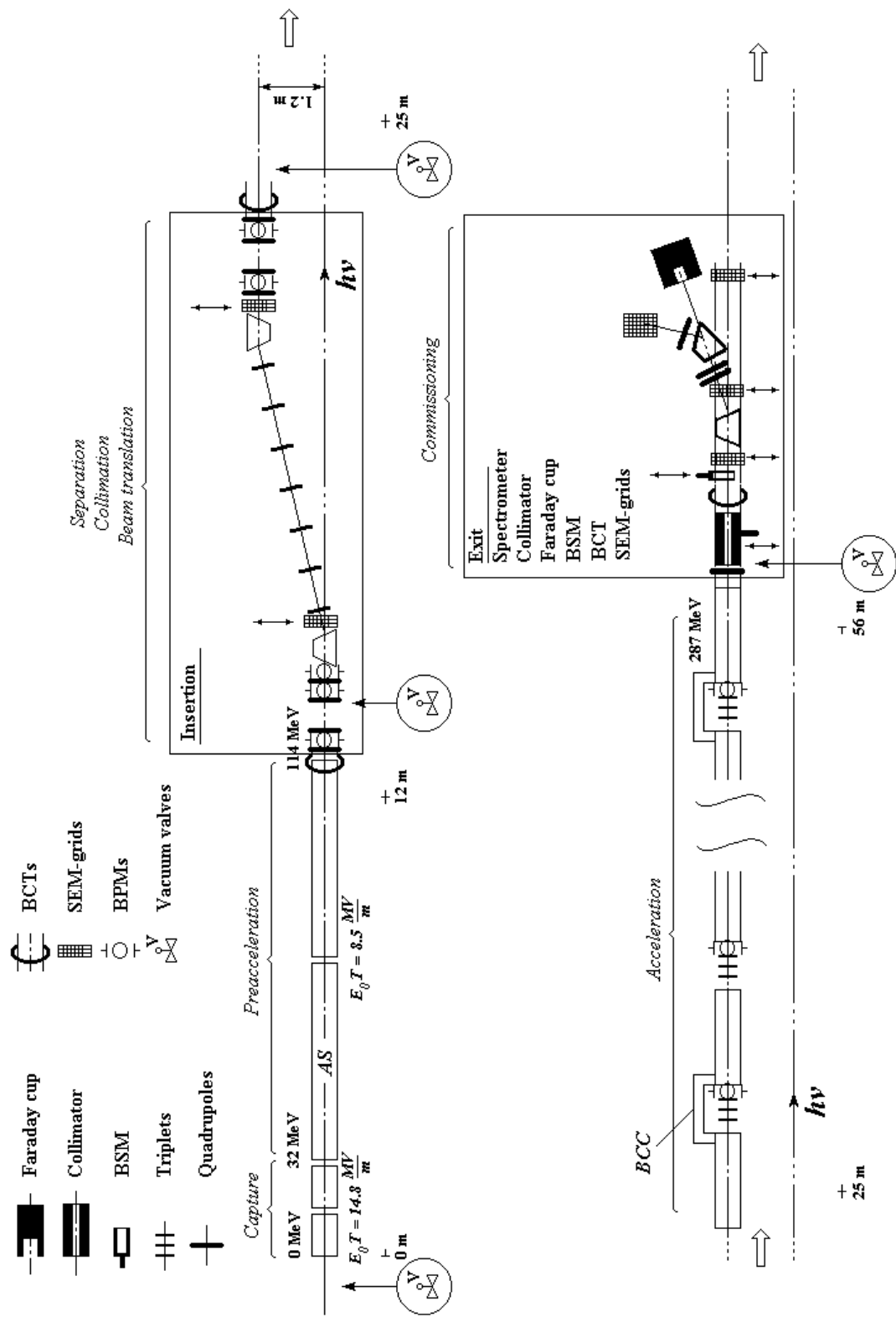
Figure 7.1. The general PPA scheme.

Table 7.1.2: Accelerating sections parameters

Section type	Type ♯1	Type ♯2	Type ♯3
Number of sections	2	2	10
Number of cells per section	11	37	19
Accelerating gradient $E_0 T$, MV/m	< 14.5	< 8.5	< 8.5
Shunt impedance Z_{sh}, MΩ/m	33.15	37.76	37.76
Transit time factor T	0.78314	0.80128	0.80128
Length, m	1.2684	4.2663	2.1908
Dissipated power, MW	< 8.04	< 8.17	< 4.15
Aperture diameter, mm	47	46	46

Table 7.1.3: The first PPA part basic parameters

Solenoid length, m	∼ 11.4
Solenoid magnetic field, T	0.22
Acceptance, m	∼ 0.037
Number of rf-sections	4
Intersection space, cm	∼ 23.06
Number of klystrons	4
Output beam energy, MeV	∼ 115

bending part a dump system will be installed with a electron loss power capability of $(12 \div 15)$ kW.

The second PPA part. It consists of 5 Accelertating Cavities (AC). Each AC consists of two Asselerating Sections (AS), joined with a bridge coupling cavity to a single resonant system. Between sections and ACs quadrupole triplets are placed. All the ASs are identical and their characteristics are listed in Table 7.1.2 as Type ♯3. Each AC is powered by one klystron. The AS are separated by a drift space of $4\lambda_{rf}$. The basic design and operation parameters for the second acceleration part are collected in Table 7.1.5. For the chosen PPA design a macroparticle simulation was carried out. Following the concept used in [2] it will be usefull to point out some specific problems of the beam dynamics.

Particle losses. A histogram of positron and electron losses in each structure element before the separator is presented in Fig. 7.1.1 with respect to the total number of positrons and electrons emerging from the target. The first column is the particle losses in the AMD. About 65% of the positrons and 76% of the electrons will be lost in the AMD and first four ACs resulting in an additional heating.

In Table 7.1.6 the power of lost particles P_L is presented for each AS. This value is calculated as energy per second of all lost particles for the positron flux from the target providing the desired number of positrons at the PPA output.

Beam loading. The particle dynamics permits to estimate the beam loading effect for each AC. A time dependent energy extraction from the first four ACs is shown in Fig. 7.1.2. There is no essential integral consumption of energy stored in the first AC due to the energy exchange of cavity field - accelerated particles and decelerated particles - cavity field. The accelerated particles are mainly positrons while the decelerated particles are mainly electrons. Moreover, due to this effect, the first two high gradient cavities operate with a low beam loading, whereas the downstream moderate gradient cavities operate

Table 7.1.4: Separator composition and element requirements.

Matching part	length, m	~ 3
	number of quadrupoles	4
	quadrupole field gradient, kG/cm	< 0.25
	quadrupole length, cm	25
	quadrupole aperture diameter, cm	8
Bending part	length, m	~ 7
	number of dipoles	2
	dipole bend angle, deg	11
	dipole magnetic field, T	~ 0.098
	dipole central energy, MeV	~ 114
	dipole central trajectory, m	0.75
	number of quadrupoles	7
	quadrupole field gradient, kG/cm	< 0.2
	quadrupole length, cm	40
	quadrupole aperture diameter, cm	12

Table 7.1.5: The second PPA part basic parameters

Number of quadrupole triplets	9
Triplet quadrupole length, cm	15
Triplet quadrupole aperture diameter, cm	6
Distance between triplet quadrupoles, cm	7.5
Side triplet quadrupole strength, m^{-2}	9
Central triplet quadrupole strength, m^{-2}	-17.1
Quadrupole field gradient, kG/cm	< 1.7
Number of rf-sections	10
Intersection space, cm	~ 92.24
Number of klystrons	5
Final beam energy, MeV	~ 285
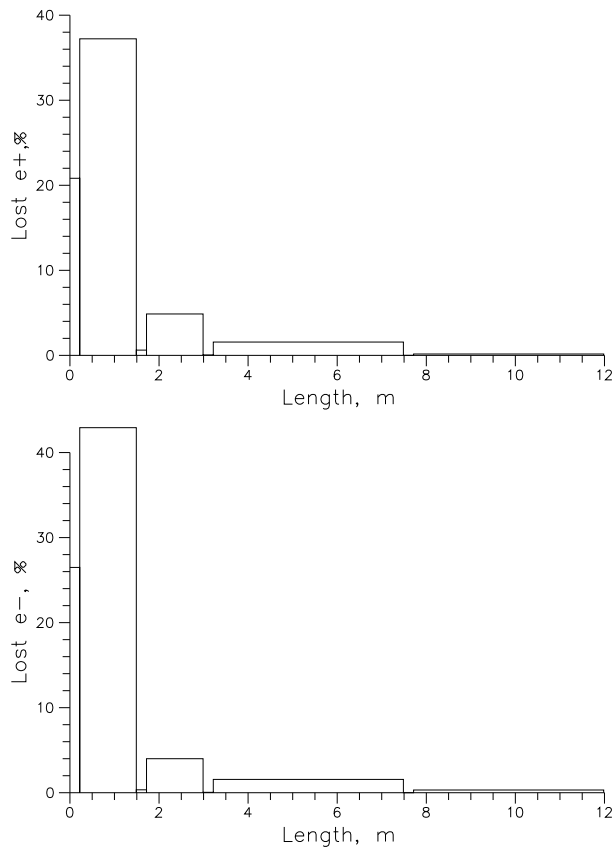
Figure 7.1.1: Particle loss distribution along the first PPA part.

Table 7.1.6: Accelerating section power performance.

P_L — power of lost particles; P_{bl}^{sep} — pulsed ($800\mu s$) beam loading power.

Section number	P_L, kW	P_{bl}^{sep}, MW
1	12.550	0.4228
2	1.2780	0.9634
3	0.6032	2.0700
4	0.0698	2.1110
5	0.5480	0.4775
6	0.0602	0.4713
7	0.0244	0.4685
8	0.0051	0.4683
9	0.0000	0.4680
10	0.0000	0.4678
11	0.0000	0.4676
12	0.0000	0.4675
13	0.0000	0.4674
14	0.0000	0.4673

Figure 7.1.2. Time dependent energy extraction from the first four AS.

with an approximately constant, high integral beam loading. In Table 7.1.6 power P_{bl}^{sep} extracted from the cavities during the operation pulse ($800\mu s$) is listed.

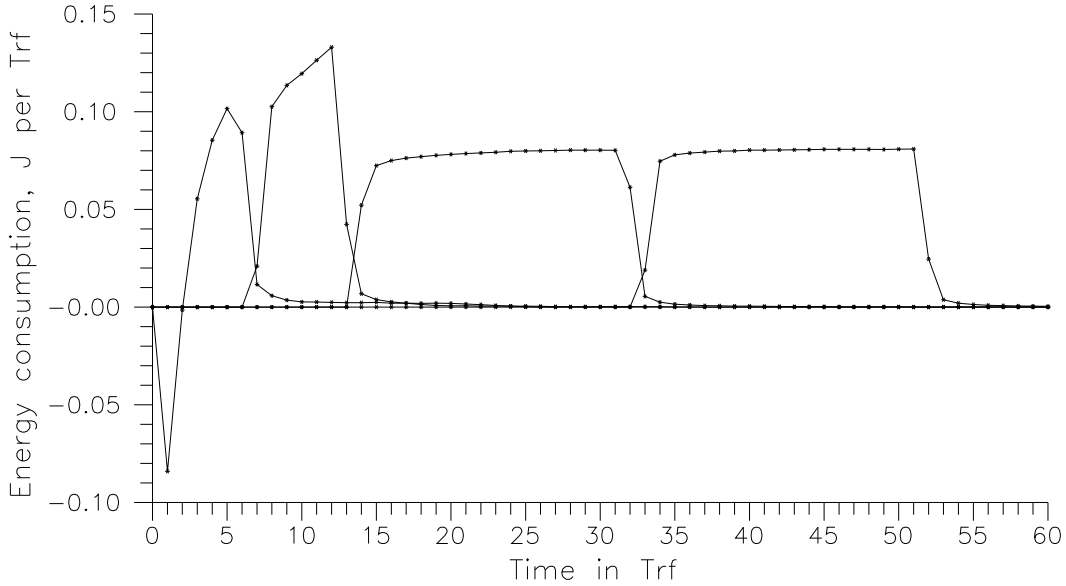<u>Positron multibunch formation.</u> In Fig. 7.1.3 a longitudinal positron phase space is shown at the PPA exit. Compared to previous simulation results [2], there is practically no multibunch structure of the output positron beam. The first positron bunch includes $\sim 99.3\%$ of the total positron number at the PPA exit.

The loss of the multibunch structure is due to two processes. First, it results from the bunch lengthening reduction at the PPA input which is done by putting the first rf-cavity into the AMD. And second, the separator nonlinear effects lead to an effective cleaning of the particles with a large deviation from the nominal energy. In Fig. 7.1.4 some output phase space portraits for the first positron bunch are presented. In the first picture the acceptable region for further acceleration is marked by a rectangle. It should be pointed out here that a more careful matching of the separator output beam with the acceptance of the second acceleration part may increase the number of positrons with a higher momentum.

A dependence of the capture efficiency as well as the optimized average beam energy at the PPA exit on the rf-phase in the second PPA part is plotted in Fig. 7.1.5. It can be concluded that the capture efficiency is stable within a wide rf-phase range less than 0°. The central energy associated with the output positron beam is well defined at a level of $\sim 285\,\mathrm{MeV}$. The basic design and operation parameters for the total PPA are collected in Table 7.1.7.

Layout and general requirements The space requirements for the updated PPA design are the same as before [2]. The total accelerator length is $\approx 60m$. It is acceptable taking into account the long distance to the main accelerator. The transverse PPA dimensions are also small and the accelerator can be easily placed in the standard TESLA tunnel together with 9 rf channels.

The reduced aperture diameter results in an increased output energy $\approx 287 MeV$ instead of $\approx 257 MeV$ [2]). Another positive consequence is the DC power consumption reduction

62
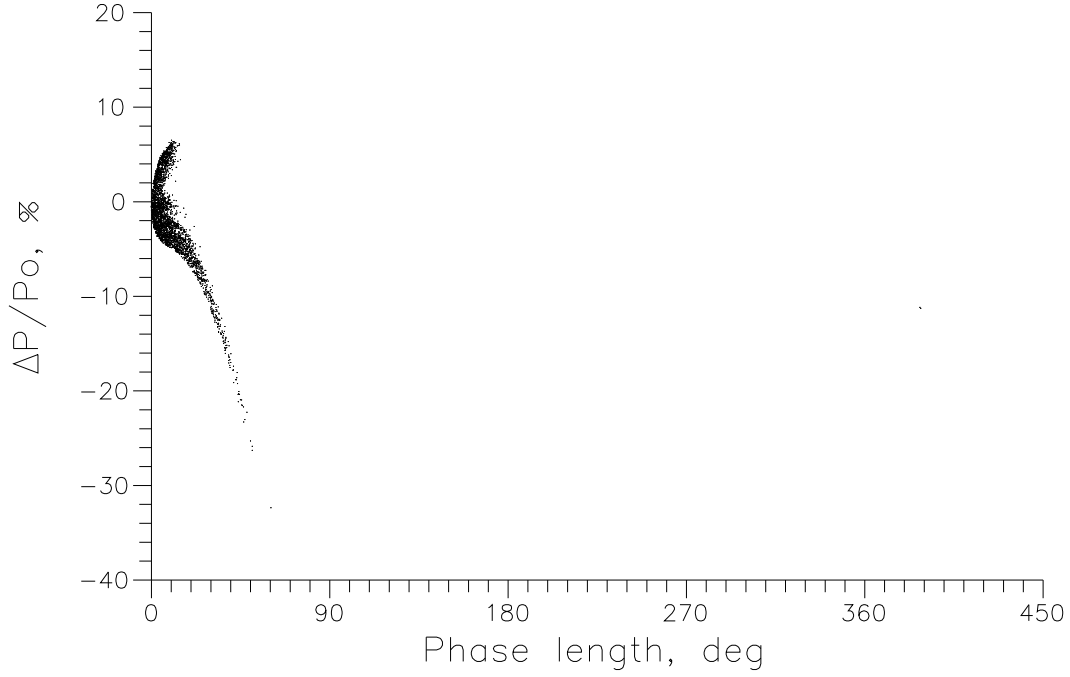
Figure 7.1.3. Longitudinal phase space of positrons at the exit of the PPA with separator.

Table 7.1.7: Basic design and operation parameters for the total PPA.

Parameter	PPA with separator
Final energy , MeV	287
Longitudinal capture efficiency, %	22.0
(for $\Delta W/W_f = \pm 6\%$; $\Delta\varphi = \pm 7.5^o$)	
Total capture efficiency, %	21.3
(for $\varepsilon_x < 0.036\,\mathrm{m}, \varepsilon_y < 0.036\,\mathrm{m}$ and $\varepsilon_x + \varepsilon_y < 0.048\,\mathrm{m}$)	
Solenoid length, m	~11.4
Solenoid field, T	0.22
Number of quadrupoles	42
Number of dipoles	2
Number of klystrons	9
Total length, m	~55.5

Figure 7.1.4. Phase space portraits of positrons at the exit of PPA with separator.

Figure 7.1.5. Capture efficiency and average beam energy vs rf-phase in the PPA output.

for focusing system (from $\approx 610kW$ to $\approx 480kW$) and related reduction in the cooling water consumption to $\approx 75m^3/h$ (without klystron cooling).
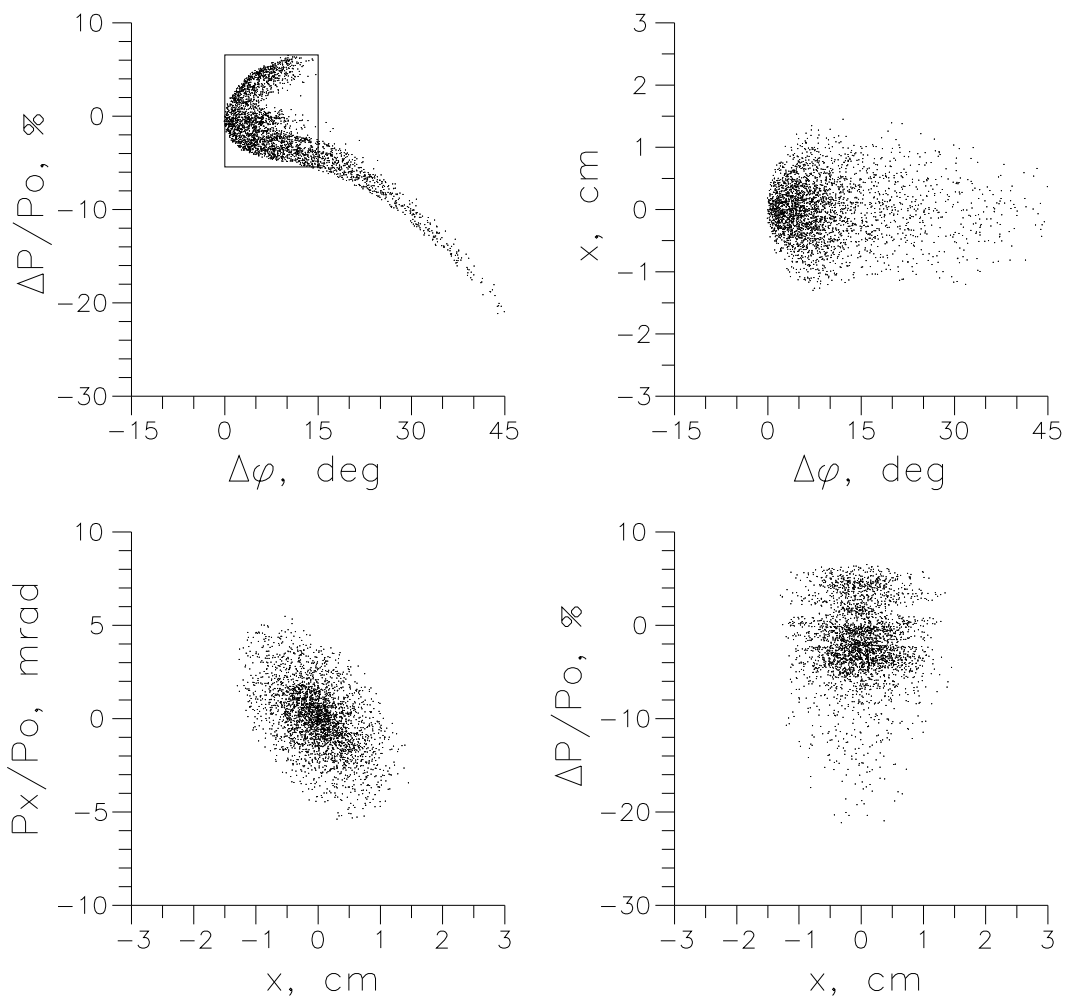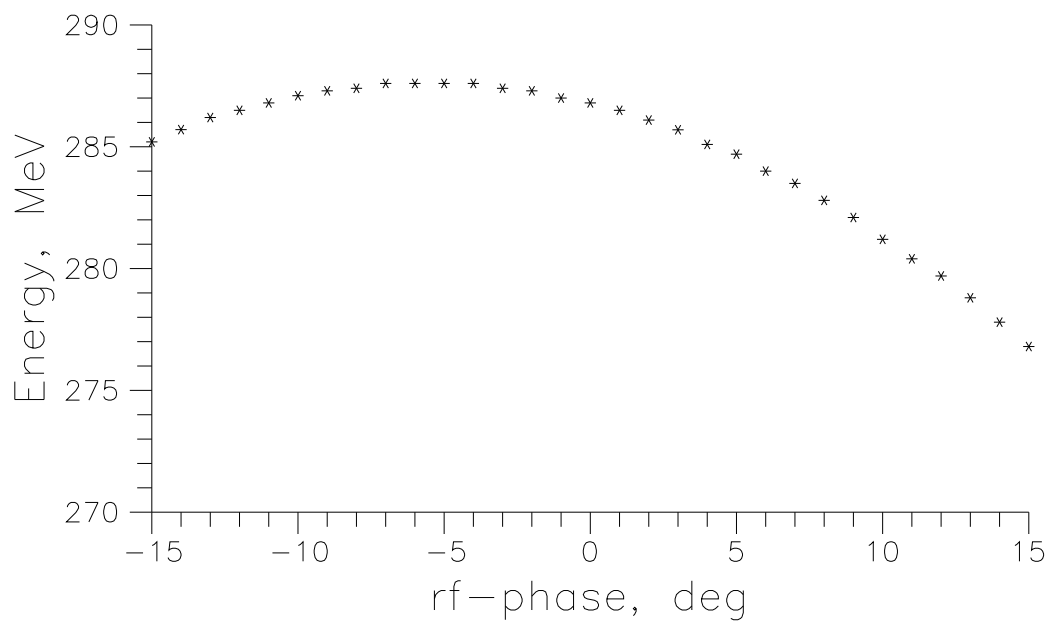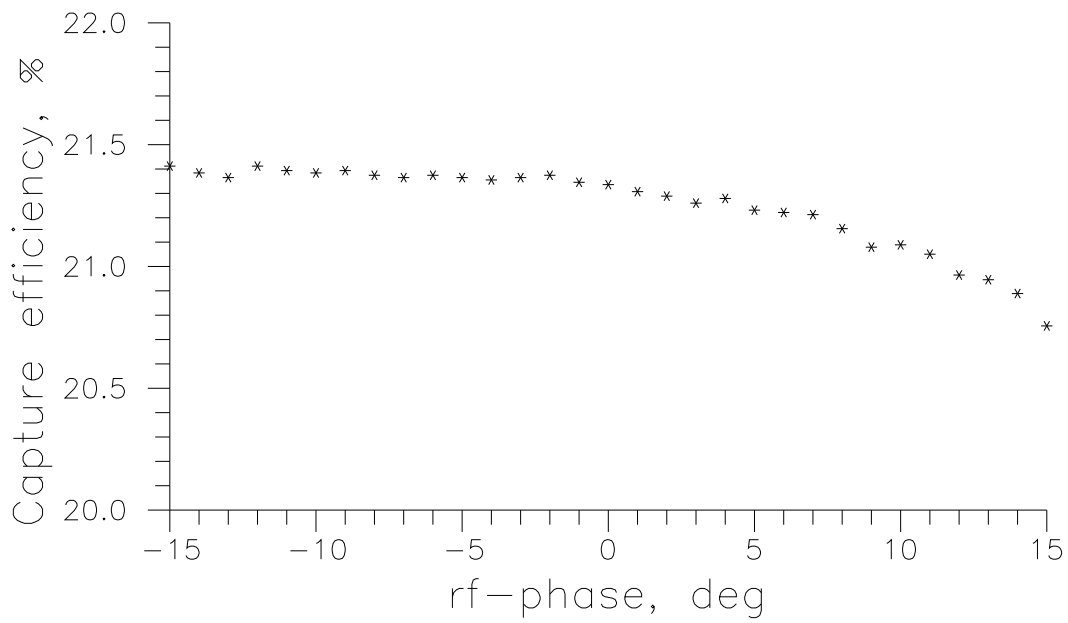
In the PPA there are at least two areas with large patricle losses - the first half of the PPA beginning and the magnetic insertion. All magnetic elements, placed in these areas - solenoid in the first PPA part, quadrupoles and bending magnets in the PPA insertion - should be made by using a special cable with mineral insulation for coils. Such cable was specially developed to operate for a long time under strong radiation conditions.

Taking into account the strong nonlinear effects in the magtetic insertion, this area should be equipped by a beam instrumentation hardware. All quadrupoles have incorporated beam position monitors. Moreover, two SEM grid monitors are forseen behind bending magnets (see Fig. 7.1) for beam profile measurements.

7.2 LPTL parameters

The LPTL structure is desrcibed in Chapter 5. The LPTL has long straight parts with FODO cells (see Fig. 5.1) and two bypass arcs. Matching sections take place between the LPTL parts, at the LPTL beginning and at the LPTL exit. Below some LPTL design details are discussed.

7.2.1 LPTL magnetic elements

Parameters of the LPTL magnetic elements are distributed in Tables 5.2 - 5.5 (Chapter 5). In the Table 7.2.1 LPTL quadrupoles parameters are summarized to represent the general LPTL structure. Special attention has been payed to minimize the variety of the quadrupole types and all LPTL quadrupoles have the same dimensions, differing only in the gradient G_0.

The DC power consumption P_{DC} for a quadrupole lens can be estimated as:

$$P_{DC} = 0.64 k_1 k_2 k_3^2 \rho \frac{l}{S} G_0^2 a^4, [W], \tag{25}$$

where a [m] - is the aperture radius, ρ - is the resistance of the winding material, l [m] - is the length of the winding turn, $S [m^2]$ - is the square of the copper cable. k_1 - is the filling coefficient, the ratio of the total window square to the square filled with copper. Usual k_1 value is $2.5 \div 3.5$ which takes into account space for cooling channels, insulation and so on. The k_2 coefficient takes into account the winding resistance increasing with the heating. A usual k_2 value is $1 \div 1.1$. Coefficient k_3 takes into account saturation effects and depends on the fiels inductance and the pole shape. Usual k_3 value is $1 \div 1.07$.

As one can see from Table 7.2.1, all the LPTL quadruplose have a rather moderate gradient and the maxumum field at the poles is far below saturation. The LPTL quarupoles can be devided in two groups - with low gradient $G_0 \leq 0.3T/m$, (211 units) and with moderate gradient $0.3T/m \leq G_0 \leq 1.5T/m$ (65 units). The DC power required for one FODO low gradient quadrupole $G_0 = 0.2T/m$ is $\approx 60W$ and such lenses can be made without water cooling to reduce costs. For DC powering several such lenses should be joint in a group to drive them from one power supply. The moderate gradient quadrupoles can be done with the same iron yoke, but winding cooling is nesessary. In should be pointed out here, that areas with such lenses are localized in the bypass and matching sections - sort sections

Table 7.2.1 LPTL quadrupoles parameters

Name	Effective length, m	Strength, $1/m^2$	Gradient, T/m	x_{max}, m	y_{max}, m	Radius of apert., m	Number
Match. section 1							
q1m1	0.5	+0.6111415	+0.5861042			0.08	1
q2m1	0.5	-0.3754501	-0.3600686			0.08	1
q3m1	0.5	-0.7896255	-0.7572761			0.08	1
q4m1	0.5	+0.6072866	+0.5824073			0.08	1
FODO cells							
	0.5	±0.2034218	± 0.1950880	0.047	0.047	0.08	206
Match. section 2							
q1m2	0.5	+0.8125865	+0.7792964			0.08	2
q2m2	0.5	-1.1596300	-1.112122			0.08	2
q3m2	0.5	+0.6900151	+0.6617465			0.08	2
q4m2	0.5	-0.2254244	-0.2161892			0.08	2
Bypass cell							
q1	0.5	-1.4929970	-1.4318320	0.013	0.022	0.08	8
q2	0.5	+0.8935150	+0.8569094	0.027	0.019	0.08	8
q3	0.5	-1.3556050	-1.300069	0.017	0.068	0.08	8
q4	0.5	+0.8769116	+0.8409862	0.035	0.021	0.08	8
q5	0.5	-1.1762750	-1.1280850	0.021	0.022	0.08	4
Match. section 0							
q2m0	0.5	+1.013745	+0.9722139	0.027	0.008	0.08	4
q3m0	0.5	-1.464863	-1.404850	0.013	0.023	0.08	2
Match. section 3							
q1m3	0.5	+0.7402444	+0.7099180			0.08	2
q2m3	0.5	-0.6277262	-0.6020095			0.08	2
q3m3	0.5	-0.2445018	-0.2344850			0.08	2
q4m3	0.5	+0.3989359	+0.3825923			0.08	2
Match. section 6							
q1m6	0.5	+0.6769593	+0.6492256			0.08	1
q2m6	0.5	-1.0072680	-0.9660022			0.08	1
q3m6	0.5	+0.4512171	+0.4327316			0.08	1
q4m6	0.5	-0.2871149	-0.2753524			0.08	1

in comparison with the total LPTL length. The transverse quadrupole dimensions are rather moderate - the lens diameter is less than 55 cm and the LPTL can be placed easyly in the TESLA tunnel.

Some lenses should be equipped with correction coils. The number and placement of such lenses should be clarified during the technical design. The moderate gradient quadrupoles are placed in the bypass and matching sections. Enlarged particle losses are possible in these areas and the necessity of a special mineral insulation for the windings should be studied also.

Parameters of the 16 identical bending magnets are listed in Table 5.4. The magnets have rather conservative parameters also. The DC power consumption for each bending magnet is $\approx 5kW$.

The total LPTL DC power consumption is estimated as $\approx 230kW$ and $10m^3/h$ cooling water consumption.

7.2.2 LPTL beam instrumentation

. The purpose of the beam diagnostics for the LPTL is to provide a sufficient amount of information about positron beam parameters during both LPTL conditioning and routine operations. A general LPTL scheme is given in Fig. 5.1 and beam parameters are described in Table 5.1. For the positron beam time structure the same parameters as in [2] are assumed.

For measurements of basic positron beam parameters such as beam position, profile, current, bunch length, energy, and beam loss both intercepting and nonintercepting techniques should be used.

The positron beam has a maximun and minimum density and a minimum and maximun size correspondingly in the matching sections and in the arcs. The beam transverse size grows up in the arcs (see Fig. 5.5 - Fig. 5.9). Therefore the beam instruments for beam parameter measurements must be grouped in these parts of the LPTL. For measurements one should use Beam Current Transformers (BCT), Beam Position Monitors (BPM), Secondary Emission Grids (SEM-grid), longitudinal Bunch Shape Monitors (BSM). These monitors are of the same types as those discussed for the PPA previously [2].

Beam intensity and position measurements. With the help of BCTs installed before matching sections (see Fig. 5.1) M1, M3, M5 and behind M2, M4, M6 it is possible to measure the bunch charge and to check the positron beam intensity transmission of all the LPTL parts. For this purpose it is reasonable to use BERGOZ ICT transformers [17] or beam transformers designed for the bunch charge measurements of LEP. The charge measurements accuracy is better than 1% [18] and does not depend on the beam position. For the beam position measurements it is necessary to use button pickups (BPM) [19]. Beam position measurements are necessary in a few FODO cells behind M1, M3, M5 and in a few FODO cells before M2, M4, M6 in order to correct the beam trajectory in the LPTL straight parts and the beam input and output directions in arcs. Knowing the beam trace up to the magnets of the arcs and the pathway behind it, it is possible to estimate the energy of a beam accelerated in the PPA. It is necessary to have BPMs in several points of the long LPTL straight parts for initial adjustment and routine activities. Beam position measurements with a resolution of $\pm 0.1mm$ can be done by nonresonant BPMs developed for TESLA [19].

Transverse profile measurements. The measurements of transverse profiles are necessary

Table 7.2.3: The list of beam monitors for LPTL beam instrumentation

Monitor	Quantity	Placement	Designation
BCT	6	at entrances of the LPTL parts	beam charge
BPM	68	every 2 FODO cells and 24 in 6 matching sections	beam position
SEM-grid	20	matching sections, arcs	beam size and position
BSM	1	LPTL exit	bunch shape and length

in a few points of M1, M6 and bypass for defining not only beam sizes but emittance as well. As a profile detector both secondary emission multiwire chambers (SEM-grid) and thin metal foils - for transient radiation generation (OTR) [20], [21] can be utilized. The preferable solution is the system based on multiwire SEM-grid. In these monitors there are no segments, aging fast in radiation fields, such as optical windows and lenses of optical channels. It is reasonable to realize a SEM-grid with input-output mechanics. Taking into consideration that the beam density doesn't reach a dangerous thermal emission limit, it is easy to see, that a SEM-grid with a thin wire diameter of about $20\mu m$ made of tungsten or carbon and with a spacing of 2 mm will disturb the beam parameteres only slightly. The SEM-grid reliability and durability are well-known. Methods of data-processing for these monitors are also perfectly worked out.

Transverse Emittance Measurement. Taking into account, that the transport line has a large length, measurements of beam emittance can be taken by the method of a few profiles.

Measurement of energy and energy spectrum of the positron beam. Measurements of energy and energy spectrum of the beam are made at the PPA exit by means of a special measuring station [2], with a spectrometer based on a dipole magnet. The same procedure with the same equipment can be applied to the LPTL exit.

Longitudinal profile and bunch duration measurements. Metal foil detectors of a profile can be used for measurements of a longitudinal bunch shape by means of a streak chamber at optical transition radiation. But the cost of a streak chamber, which gives a resolution of $1 \div 2ps$, is very high, therefore it is easier and cheaper to use for this purpose a longitudinal bunch shape monitor on the basis of a wire probe [2]. This monitor should be installed at the exit of the LPTL.

The LPTL beam parameter measurement system . The subsystems of beam monitors, discussed above, are integrated into a joint LPTL beam parameter measurement system. These subsystems are mainly useful during the LPTL commissioning. The BCT subsystem has 6 BCTs in 6 matching sections, where the beam has the smallest transverse sizes. BERGOZ manufactures BCTs and preamplifiers with generators of calibration signals for these transformers [17]. The BCT system gives a picture of the beam intensity transmission from the entrance of the LPTL to its exit.

The beam position monitors (BPM) are installed in quads of the first two FODO cells behind M1, M3, M5, and in quads of the last two FODO cells in front of M2, M4, M6. Additional BPMs can be installed every 50 m in the quadrupoles of long lines. BPMs should be constructed on the basis of buttons $15mm$ in diameter. BPMs should also be protected from hits of particles of a beam and secondary radiations by segments of the vacuum chamber.

4 Beam profile Monitors may be installed behind every quad of M1 for emittance mea-

Table 7.3.1 MPA general parameters.

Parameter	Basic design	Proposal with long doublets
Cryomodule ♯1		
Number of cryomodules	8	8/22
Cryomodule length,m	11.368	11.368
Energy gain per cryomodule, MeV	100	100/175
Number of quadrupole doublets	4	4/1
Number of accelerating sections	4	4/7
Cryomodule ♯2		
Number of cryomodules	20	0
Cryomodule length,m	12.352	-
Energy gain per cryomodule, MeV	200	-
Number of quadrupole doublets	1	-
Number of accelerating sections	8	-
Final beam energy, GeV	~ 5.08	~ 4.93
Total length, m	~ 338	~ 341
Safety factor	> 2	> 2
Total number of klystrons	6	6.5
Total number of cryomodules	28	30
Total number of quadrupole doublets	52	54
Total number of accelerating sections	192	186

surements and in front of 4 quads of M6, because a beam emittance can increase in the long line due to scattering on residual gas.

The SEM-grids are mounted in front of M2, M4, and behind M3, M5. They are also installed behind the first, third, fifth and seventh dipoles of the arcs for adjustment of the beam size during the LPTL commissioning.

The bunch shape monitor is installed behind the collimator before M6.

Table 7.2.3 gives the list of beam monitors.

7.3   Main Positron Accelerator design.

According to the studies presented in Chapter 6 the MPA structure can be constructed from the two types of the standard TESLA cryomodules. The transverse focusing is carried out by quadrupole doublets. The schematic view and element position of the MPA are given in Fig.7.3.1. The general parameters are collected in Table 7.3.1, the safety factor being calculated as the ratio of the element inner radius to the maximum beam envelope in this element. The beam radius corresponds to the transverse emittances $\varepsilon_x = \varepsilon_y = 0.036$ m. The second variant of the MPA design in Table 7.3.1 is referred to the realization with a long quadrupole construction mentioned at the end of Chapter 6. To fulfil the rf-feeding standard TESLA klystrons and rf-elements are suggested [1].

Figure 7.3.1. MPA schematic view.

8 Conclusions

The present report summarizes the results of the design study for the total TESLA positron injector line. This line consists of several essentialy different parts - a normal conducting Positron Pre-Accelerator, a Long Positron Transport Line with bypass sections and a superconducting Main Positron Accelerator. Parameters both of each part and the total line are otimised in order to obtaine scientifically effective, technically reasonable and cost saving solutions.

The PPA is a standing wave normal conducting linac. All solutions for the PPA systems base on experience of exsisting linear accelerators with usage of standard TESLA RF equipment.

The LPTL structure is adequate to unique beam parameters. The LPTL magnetic elements have conservative cost-saving parameters.

The MPA is designed consisting of standard TESLA equipment.

The total transmission of the line for the positron beam is estimated as $\approx 16\%$. This value is sufficient to provide the required positron number for the TESLA luminosity. Improvements of the transmission coeffiient seem to be possible with a more careful LPTL design taken into account nonlinear effects.

References

[1] Conceptual Design of a 500 GeV e^+e^- Linear Collider with Integrated X-ray Laser Facility. DESY 1997-048

[2] K. Flöttmann, V. Paramonov (ed.) Conceptual design of a Positron Pre-Accelerator for the TESLA Linear Collider, TESLA 99-14, DESY, 1999

[3] K.Flöttmann, Investigations Toward the Development of Polarized and Unpolarized High Intensity Positron Sources for Linear Colliders, DESY 93-161, 1993.

[4] V.V. Paramonov, The Cut Disk Structure for High Energy Linacs, Proc. 1997 PAC, v.3, p. 2962. 1998. V.V. Paramonov, L.V. Kravchuk, V.A. Puntus, The cold model of the CDS structure, Proc. 1998 Linac Conference, ANL-98/28, p.579.

[5] E.A. Knapp et al, Standing wave high energy accelerating structures, Rev. of Sci. Instr. v. 39, p. 979, (1968)

[6] Y. Morozumi et al, Multi-Cavity Bridge Coupler, Proc. of the Linac 90 conference, p.153.

[7] V.G. Andreev et al, Bridge Device for Cavities of a Proton Linac..., RTI, Moscow, N20, p47, 1974 (in Russian).

[8] V.G. Andreev et al, Results of the high power test, RTI, Moscow, N25, p123, 1976 (in Russian).

[9] R.L. Sheffield at. al. High-Brightness linac for the Advanced Free-Electron Initiative at Los Alamos. Proc. of the 1992 Linac Conf., v.1 p. 46, 1993. R.L. Sheffield at. al. Operation of the High-Brightness linac ... . Proc. of the 1995 PAC Conf., p. 2970, 1995.

[10] M.F.Vorogushin, V.N. Malyshev, RF systems of resonant accelerators for applied purposes. Energoatomizdat, Moscow 1989, (in Russian)

[11] V.A.Moiseev, P.N.Ostroumov, Code to Study the High Intensity Beam Dynamics in the Ion Linear Accelerators, Proc. of the VI European Particle Accelerator Conference (EPAC-6), Stockholm, Sweden, pp.1216-1217, 1998.

[12] V.V. Balandin, N.I. Golubeva, Hamiltonian Methods for the Study of Polarized Proton Beam Dynamics in Accelerators and Storage Rings. DESY Report 98-016, DESY, Hamburg, 1998

[13] B.W.Montaque, Chromatic effects and their first-order correction, CAS, vol.1, Geneva, pp.75-90, 1987.

[14] K.G.Steffen, High Energy Beam Optics, Interscience publishers, New York, 1965.

[15] N. Golubeva, A. Iliev, Yu. Senichev. A racetrack lattice with missing magnets for the Booster, TRIUMF design note, TRI-DN-91-K188.

[16] H.H.Braun et al.. The CLIC RF Power Source. A Novel Scheme of Two-Beam Acceleration for Electron-Positron Linear Colliders, CERN 99-06.

[17] BERGOZ price list, 1995.

[18] K.B. Unser, Measuring Bunch Intensity, Beam Loss and Bunch Lifetime in LEP, Proc. EPAC-90, p. 786.

[19] K. Yezza, et al., Beam Position Monitor Developments for TESLA, Proc. EPAC-94, p.1533.

[20] M. Bernard et al., The TESLA Test Facility Linac Injector, Proc. EPAC-94, p. 692.

[21] J.-C. Denard et al., High Power Beam Profile Monitor with Optical Transition Radiation, Proc. PAC-97, p.2198.

[22] D.A. Edwards (ed.) TESLA Test Facility Linac Design Report, TESLA 95-01, DESY, 1995

[23] S.Wolff, Private communication, DESY, November 1999.